Preparation and characterization of SnSe thin films for gas sensing application

Dissertation submitted to
Visvesvaraya National Institute of Technology, Nagpur
in partial fulfilment of the requirements for the award of the degree

Master of Science

in

Physics

by

AMAN KUMAR GILL
(MS23PHY005)

under the guidance of
Dr. G. Hema Chandra

Department of Physics
Visvesvaraya National Institute of Technology
Nagpur (440010) India

May 2025

Preparation and characterization of SnSe thin films for gas sensing application

Dissertation submitted to
Visvesvaraya National Institute of Technology, Nagpur
in partial fulfilment of the requirements for the award of the degree

Master of Science

in

Physics

by

AMAN KUMAR GILL
(MS23PHY005)

under the guidance of
Dr. G. Hema Chandra

Department of Physics
Visvesvaraya National Institute of Technology
Nagpur (440010) India

May 2025

© Visvesvaraya National Institute of Technology (VNIT) 2009

Department of Physics

Visvesvaraya National Institute of Technology, Nagpur

Dissertation Approval Sheet

The dissertation titled "**Preparation and characterization of SnSe thin films for gas sensing application**" submitted by Mr. Aman Kumar Gill has been approved for the fulfilment of the degree of Masters of Science in Physics.

_____ _____

(Name: Dr. G. Hema Chandra) (Name:)

Supervisor **External Examiner**

_____

(Name:)

Chairman

Date:

Place: Nagpur

Department of Physics
Visvesvaraya National Institute of Technology, Nagpur

Declaration

I, **Aman Kumar Gill**, hereby declare that this dissertation titled "**Preparation and characterization of SnSe thin films for gas sensing application**" is carried out by me in the Department of Physics of Visvesvaraya National Institute of Technology, Nagpur. The work is original and has not been submitted earlier whole or in part for the award of any degree/diploma at this or any other Institution / University.

Aman Kumar Gill
Date:

Certificate

This to certify that the dissertation titled "**Preparation and characterization of SnSe thin films for gas sensing application**" is submitted by **Aman Kumar Gill** in partial fulfilment of the requirements for the award of the degree of **Master of Science in Physics**, VNIT Nagpur. The work is comprehensive, complete and fit for final evaluation.

Dr. G. Hema Chandra
Professor
Department of Physics
VNIT, Nagpur

Head, Department of Physics
VNIT, Nagpur
Date:

Department of Physics
Visvesvaraya National Institute of Technology, Nagpur

Non-Plagiarism Certificate

Certified that M.Sc. dissertation titled "**Preparation and characterization of SnSe thin films for gas sensing application"** submitted by **Aman Kumar Gill**, Enrollment no. **MS23PHY005** And ID No. **30108** has been checked for plagiarism using TURNITIN and overlap is found within prescribed limits. A summary of report given below:

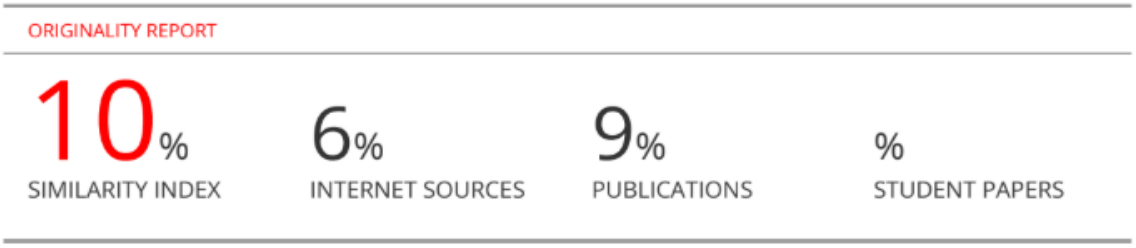

Aman Kumar Gill
(MS23PHY005)
ID No: 30108

Dr. G. Hema Chandra
Professor,
Department of Physics.

Acknowledgements

I would like to express my sincere gratitude to **Dr. G. Hema Chandra**, Professor, Department of Physics, Visvesvaraya National Institute of Technology, Nagpur, for providing me the opportunity and for his guidance to carry out the M.Sc. project under him. It was a great experience for learning and I gained invaluable insight into the semiconductor devices and their fundamentals.

I would like to thank **Dr. B.R. Sankapal**, Head of Department of Physics, VNIT and **Dr. Prem Lal Patel**, Director, VNIT, for providing me necessary facilities for the completion of my project work.

I am extremely grateful to **Mr. Yashpal Pawar** and **Shreosi Mukherjee,** Research scholar, Department of Physics, VNIT, for his relentless support and valuable advice throughout the duration of my project.

I would like to thank my classmates **Akankshya Pati** and **Ramachandra Shinde** for their support and help.

I am extremely grateful to my parents and family members, without their support and nurturing, the completion of my project would not have been possible.

AMAN KUMAR GILL

ABSTRACT

Thin film gas sensors fabricated with the deposition of *p*-SnSe thin film onto the silver electrodes coated glass substrates to sense hydrocarbon types of gases like LPG and to test the material for thermoelectric properties as it was reported as a good thermoelectric material. So, to understand the parameters that affect the sensitivity of a gas sensor of SnSe thin film towards the hydrocarbon type gases is still required. Since we used the thermal evaporation technique, the parameters that can be altered are deposition rate, substrate temperature and film thickness. The film thickness was taken to be 600 nm, the rate varied from 2 to 2.5 Å/s, substrate temperature varied from RT to 200 ˚C. After that different characterization was carried out of deposited SnSe thin film by X-Ray diffraction, Raman, Field Emission Scanning Electron Microscope (FE-SEM), Energy Dispersive X-Ray spectroscopy, UV-Vis and Hall effect measurement set up. By those results it was found that there was a single-phase present at lower deposition temperatures and binary phase present at higher temperatures. By the Hall effect measurement, it was found that the hole mobility of *p*-SnSe was varied from 0.27 to 15.47 cm^2/V-s, the carrier concentration was varied from 10^{16} to 10^{18} of orders. By UV-Vis, the optical band gap was varied from 1.29 to 1.08 eV of *p*-SnSe from RT to 200 ˚C of substrate temperature. The Seebeck coefficient for *p*-SnSe was varied from 3.7 mV/˚C to 0.18 mV/˚C for 100 ˚C and 200 ˚C respectively. After that, the gas sensing properties like sensitivity was observed for *p*-SnSe deposited at 200 ˚C for 60 ˚C and 90 ˚C of sensor temperature and sensitivity were found to be varied from 2.35% to 19.12%.

CONTENTS

Abstract

Contents

List of Figures

List of Tables

List of Abbreviations

List of Symbols

1. INTRODUCTION

1.1. Need of air pollutant

1.1.1. Different methods to sense a gas

1.2. Synthesis of Gas sensors

1.2.1. Different gas sensing materials

1.2.1.1. Thin film gas sensors

1.2.1.2. Thick film gas sensors

1.3. Thermoelectric materials

1.4. Thermoelectricity

1.4.1. Thermoelectric effect

1.4.2. Seebeck effect

1.4.3. Peltier effect

1.5. Properties of thermoelectric materials

1.5.1. Heat transfer

1.5.2. Figure of merit

1.5.3. Electrical transport

1.6. IV-VI based gas sensors

1.7. SnSe thin film-based gas sensors

2. LITERATURE REVIEW

2.1. Synthesis, characterization and properties of SnSe thin films

3. EXERIMENTAL WORK

3.1. Thermal evaporation technique

3.2. Components of thermal evaporation system

3.2.1. Vacuum coating unit

3.2.1.1. Rotary pump

3.2.1.2. Diffusion pump

3.2.1.3. Pirani gauge

3.2.1.4. Penning gauge

3.2.2. Resistive heater

3.2.3. Quartz thickness monitor

3.2.4. Substrate holder

3.2.5. Shutter

3.2.6. Water cooling system

3.2.7. Gas mass flower

3.3. Deposition of SnSe thin films

3.3.1. Substrate cleaning process

3.3.2. Tooling factor

3.3.3. Variation in substrate temperature

4. CHARACTERIZATION TECHNIQUES

4.1. XRD (X-Ray Diffractometer)

4.2. Raman spectroscopy

4.3. SEM-EDX (Scanning Electron Microscope and Energy Dispersive X Ray spectroscopy)

4.4. UV-Visible spectroscopy

4.5. Optical profiler

4.6. Hall effect measurement

5. RESULTS AND DISCUSSION

5.1. XRD analysis

5.2. Raman analysis

5.3. Morphology and Compositional analysis

5.4. Optical analysis

5.5. Thickness analysis

5.6. Electrical analysis

5.7. Thermoelectric measurements

6. APPLICATIONS

6.1. Gas sensor

6.1.1. Temperature variation during measurements

6.1.1.1. At a temperature of 60 ˚C

6.1.1.2. At a temperature of 90 ˚C

6.1.2. Discussion on sensing results

7. CONCLUSION

7.1. Summary

7.2. Conclusion

7.3. Future scope

LIST OF FIGURES

Figure No.	Title	Page No.
1	Different gas sensors based on their different working principles	3
2	Schematic of a Chemi-resistive gas sensor with finger like electrode	3
3	Schematic of thick film using screen printing	4
4	Equipment component of total fabrication costs is increasing much faster than land and buildings	5
5	Different ZT values for different materials as a function of developing year	6
6	A Seebeck effect is shown by using a thermocouple and multimeter	7
7	Schematic of a thermoelectric module for refrigeration mode (and called a Peltier cooler) or in power generation mode (and called a thermoelectric generator)	8
8	Schematic of Seebeck coefficients Vs Temperature of metal and semiconductor	11
9	Various applications of metal selenides and sulphides	12
10	Schematic of Thermal evaporator system	16
11	Schematic of Rotary pump	17
12	Schematic of Diffusion Pump	18
13	Schematic of Pirani Gauge by Wheatstone bridge setup	19
14	Schematic of Penning Gauge	20
15	Quartz crystal and its connections for thickness monitor	21
16	3 Substrates loaded in substrate holder with mica mask on the substrates for pattering	21
17	Finger type Ag electrodes deposited on the glass substrate by using mica mask	23
18	SnSe deposited for gas sensing device with silver electrodes	24
19	Thermal Evaporation Machine	24

20	Geometry for XRD	25
21	Schematic of XRD	27
22	X- Ray Diffractometer Instrument	27
23	Various vibrational states and different scatterings	28
24	Schematic of Raman spectrophotometer	29
25	Schematic of SEM	30
26	Different types of electrons ejected by SEM	31
27	Schematic of EDX attached with SEM	32
28	Different optical transitions	33
29	Schematic of UV-Vis Spectrophotometer	34
30	Optical profilometer	36
31	Schematic of Optical profilometer	36
32	Hall effect schematic	37
33	Van der Pauw technique	39
34	Hall Effect measurement setup for electrical measurement	39
35	XRD pattern for SnSe at different substrate temperatures	40
36	Raman spectra for SnSe films deposited at different substrate temperatures	42
37	FE-SEM images of SnSe deposited at different substrate temperatures	43
38	EDS spectra for SnSe thin film deposited at RT	44
39	Transmittance spectra for deposited SnSe thin films deposited at different substrate temperatures	45
40	Reflectance spectra for deposited SnSe thin films deposited at different substrate temperatures	45

41	Optical direct band gaps for different SnSe thin films at different substrate temperatures	46
42	Plot of thermo emf Vs ΔT of SnSe thin films deposited at different temperatures.	49
43	Diagram of response time after gas	51
44	Diagram of recovery time after the gas was ejected	52
45	Response and recovery time of a gas sensor	52
46	Gas sensing material inside the vacuum chamber	53
47	Measuring set up for gas using a pipette and a glass jar	55
48	Gas sensing setup with LPG cylinder, jar, gas sensing unit with chamber connected with rotary pump and laptop	56
49	LPG response for SnSe sensing material at 50 ppm	57
50	LPG response for SnSe sensing material at 100 ppm	57
51	LPG response for SnSe sensing material at 150 ppm	58
52	LPG response for SnSe sensing material for less than 50 ppm	59
53	LPG response for SnSe as a sensing material for different concentrations at 200 ppm, 250 ppm and 300 ppm	59

LIST OF TABLES

Table No.	Title	Page No.
1	Reference and Equivalent Methods for Air Monitoring of Criteria Pollutants	1
2	Long term and short-term limits exposure for different toxic gases	2
3	Parameters for deposited Ag electrodes	23
4	Parameters for SnSe thin film deposited on the glass substrate using SnSe powder	23
5	Average crystallite size of SnSe films deposited at different substrate temperatures	41
6	Lattice parameters for SnSe thin films deposited at different substrate temperatures	41
7	Elemental atomic percentage in deposited SnSe thin films	44
8	Thickness of deposited SnSe thin films at different substrate temperature	47
9	Electrical properties of deposited SnSe thin films at different substrate temperatures	48
10	Different Seebeck coefficients for different SnSe thin films	49
11	Different responses for LPG by taking SnSe as a sensing material at 60 ˚C at different concentrations	60
12	Different responses for different concentration of LPG gas by using SnSe as a sensing material at 90 ˚C	61

LIST OF ABBREVIATIONS

Abbreviation	Full form
Ag	Silver
In	Indium
SnSe	Tin Selenide
$SnSe_2$	Tin di-selenide
PVD	Physical Vapour Deposition
QTM	Quartz Thickness Monitor
XRD	X-Ray Diffraction
SEM	Scanning Electron Microscope
SE	Secondary electrons
BSE	Back scattered electrons
FE-SEM	Field emission Scanning electron microscope
EDX	Energy Dispersive X-Ray spectroscopy
UV	Ultra violet
Vis	Visible
NIR	Near Infra-Red
FWHM	Full Wavelength of Half Maxima
WH	Williamson Hall

LIST OF SYMBOLS

Symbol	Meaning
E_c	Conduction band energy
E_v	Valence band energy
E_g	Energy band gap
β	Full width half maxima
N_d	Donor concentration
N_a	Acceptor concentration
B	Magnetic field
I	Current
q	Charge
t	Thickness of sample
ν	Frequency
V_H	Hall voltage
ZT	Figure of merit
T	Tesla

CHAPTER 1: INTRODUCTION

1.1. NEED OF AIR POLLUTANT MONITORING

Nowadays, one of the major problems in human life is pollution. There are many types of pollutants in the air that degrade air quality. Humans inhale these pollutants along with the air, which can lead to serious health problems in the future. To address this issue, it is essential to monitor air quality, especially in healthcare centres, hospitals, and other critical public places. Some gases present in the air are extremely harmful to the human body. Hence, accurate detection of these pollutants necessitates the use of sensors capable of quantifying their concentration to assess ambient air quality and ensure respiratory safety.

In table 1, we can see the different types of gases present in the environment. The concentrations of these gases are given in both percentage and parts per million (ppm) near sea level [1].

Table 1: Typical composition of clean, dry air near the seal level [1].

Gases	Content % by volume	Content in ppm
N_2	78.09	780900
Ar	0.93	9300
O_2	20.94	209400
Ne	18×10^{-4}	18
CO_2	0.033	330
He	5.2×10^{-4}	5.2
CH_4	1.5×10^{-4}	1.5
Kr	1×10^{-4}	1
N_2O	0.5×10^{-4}	0.5
H_2	0.5×10^{-4}	0.5
Xe	0.08×10^{-4}	0.08
NH_4	0.01×10^{-4}	0.01
O_3	0.03×10^{-4}	0.03

NO_2	0.001×10^{-4}	0.001
SO_2	0.0002×10^{-4}	0.0002
I_2	0.01×10^{-4}	0.01
CO	0 to trace	-

The exposure of toxic gases is dangerous for human life not for a short time but for a long time also. In table 2, there are the limits of the gases to inhale even in their low concentrations and are harmful for our body cells.

Table 2: Long term and short-term limits exposure for different toxic gases [2] [3].

Gas	Long term exposure limit, 8 hours (ppm)	Short term exposure limit, 10 min. (ppm)
CO	50	300
H_2S	10	15
PH_3	-	0.3
SO_2	2	5
NO_x	3	5
Cl_2	0.5	1
NH_3	25	35
HCl	-	5
CH_3OH	200	250
C_3H_8	-	10000
C_4H_{10}	-	10000

1.1.1. Different methods to sense a gas

According to the different working principles, there are several methods to sense a gas. Majorly, they are divided into seven types [4].

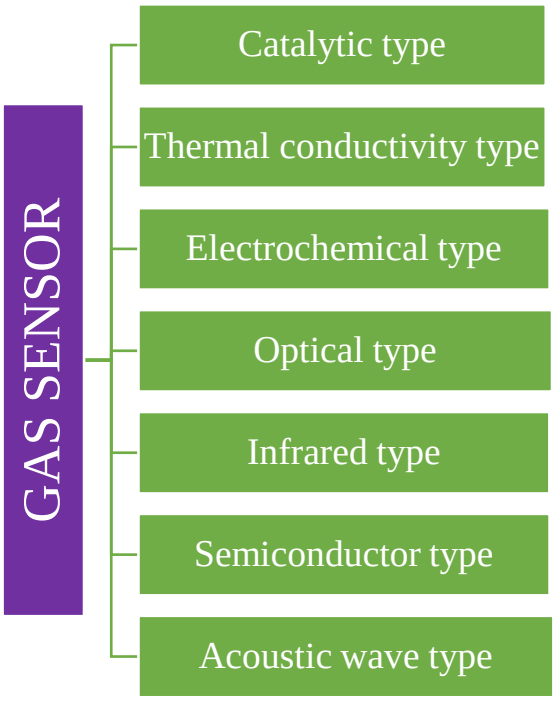

Figure 1. Different gas sensors based on their different working principles

The fundamental operation of these gas sensors is based on the variation in electrical resistance upon exposure to specific gases, whether oxidizing or reducing. These sensors are classified as chemi-resistive gas sensors. Their working principle involves the adsorption or desorption of target gas molecules on the sensing material's surface. Depending on the gas's nature, it either donates electrons to or accepts electrons from the sensing material, resulting in a measurable change in the material's electrical resistance.

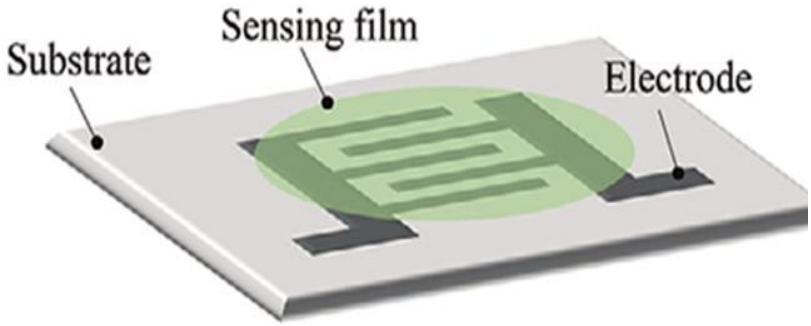

Figure 2: Schematic of a chemi-resistive gas sensor with finger like electrodes [5]

1.2. SYNTHESIS OF GAS SENSING MATERIAL

As previously mentioned, a gas sensor is a device that generates an electrical signal in response to the presence of a specific gas within a defined area. This response is primarily based on the change in electrical resistance of the sensing material upon gas exposure. Various techniques are available for fabricating gas sensing materials; however, these fabrication methods are generally classified into two main categories.

(i) Thick film deposition

(ii) Thin film deposition

1.2.1. Thick Film deposition

Thick film deposition typically refers to the fabrication of metal oxide semiconductor-based sensing layers, usually with a thickness in the micrometre range. This is commonly achieved through screen-printing technology. In this process, a paste is formulated by combining metal oxide powders with organic binders and inorganic additives, forming a chemically sensitive layer. This paste is then printed onto a substrate that contains pre-patterned metal electrodes and an integrated backside heating element. Following deposition, the printed layer is subjected to sintering typically using an infrared (IR) belt furnace to enhance its structural and functional properties [6]

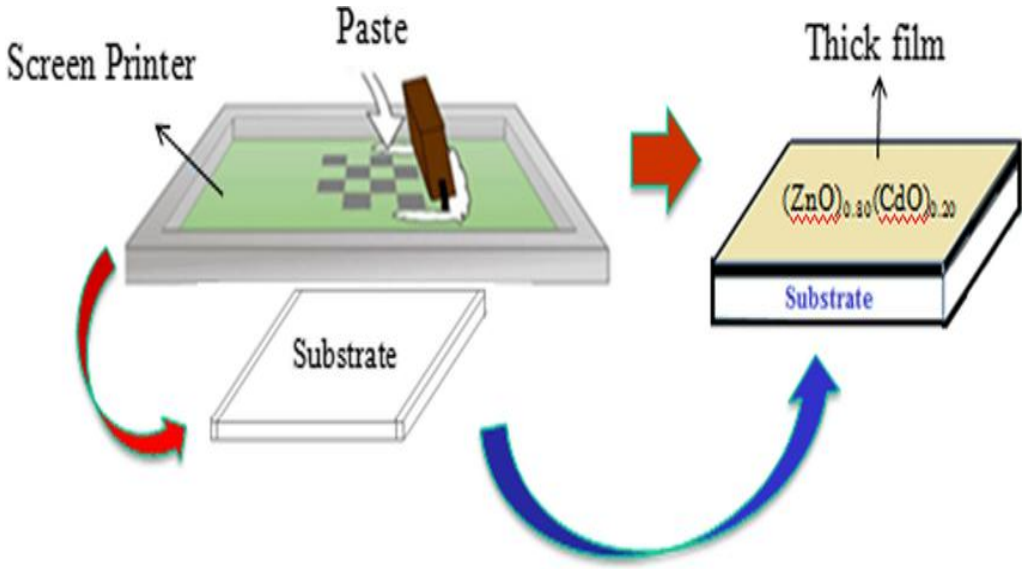

Figure 3: Schematic of thick film using screen printing, [7].

1.2.2. Thin film deposition

The graph clearly illustrates the breakdown of fabrication costs, including equipment expenses and land or building costs. It also highlights the significant growth trend in the thin film industry over time.

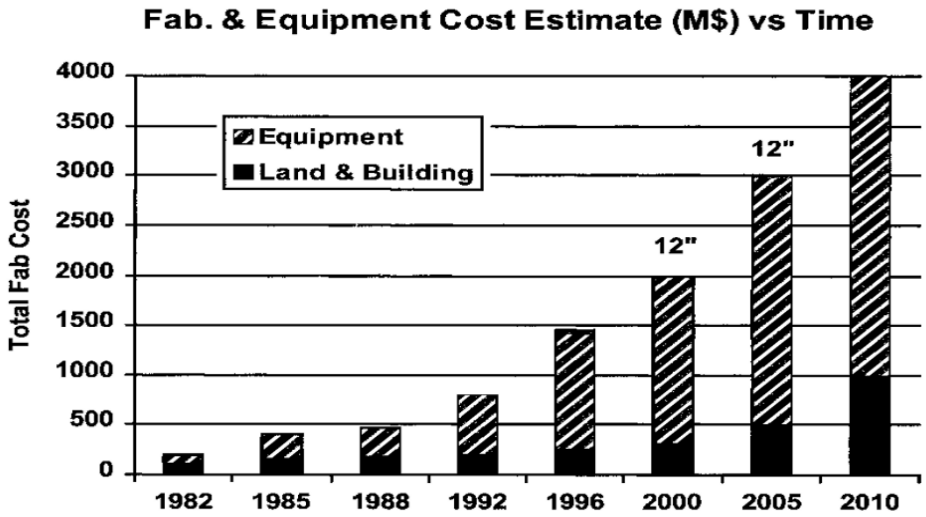

Figure 4: Equipment component of total fabrication costs is increasing much faster than land and buildings. (Source: Dataquest Report 2000.) [8]

There are various technologies available for material fabrication, but here we focus specifically on thin film fabrication, where film thickness ranges from a few nanometres up to 10 micrometres. Thin film deposition techniques can be broadly classified into two categories: physical methods and chemical methods. Physical deposition techniques do not involve chemical reactions during the film formation and are typically performed in a vacuum environment. In contrast, chemical deposition methods involve chemical reactions either during or after the film deposition process.

1.3. THERMOELECTRIC MATERIALS

Thermoelectric materials have garnered significant research interest because studies indicate that approximately 60% of energy is wasted, primarily as heat. Recovering this waste heat by converting it into electrical energy offers a promising approach to conserve fuel resources. This thermoelectric conversion process is environmentally friendly and sustainable. Although the efficiency of current thermoelectric materials remains relatively low, they still demonstrate considerable potential for energy harvesting applications. The efficiency of these materials is quantified by a dimensionless parameter known as the figure of merit, denoted as ZT [9].

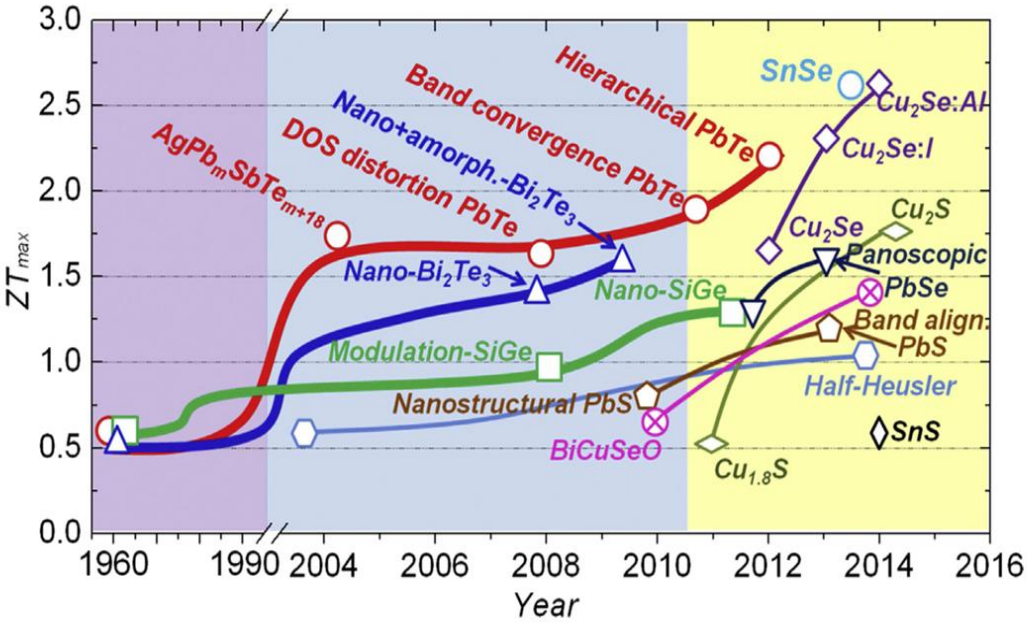

Figure 5: Different ZT values for different materials as a function of developing year [9].

1.4. THERMOELECTRICITY

1.4.1. Thermoelectric effect

The term "thermoelectric" derives from "thermo," meaning temperature, and "electric," meaning electricity. It refers to the phenomenon where a temperature difference across a material generates an electric voltage. When a thermal gradient is applied between

the two ends of a material, a potential difference is created; materials exhibiting this behaviour are known as thermoelectric materials [10].

1.4.2. Seebeck effect

This Seebeck phenomenon is a fundamental effect of the material which describes that how the charges flow by creating the temperature gradient. This phenomenon can also be understandable by mathematical formulation by introducing a coefficient known as Seebeck coefficient which is generally denoted by (S) which quantifies that how much potential difference will be created by creating per unit temperature difference.

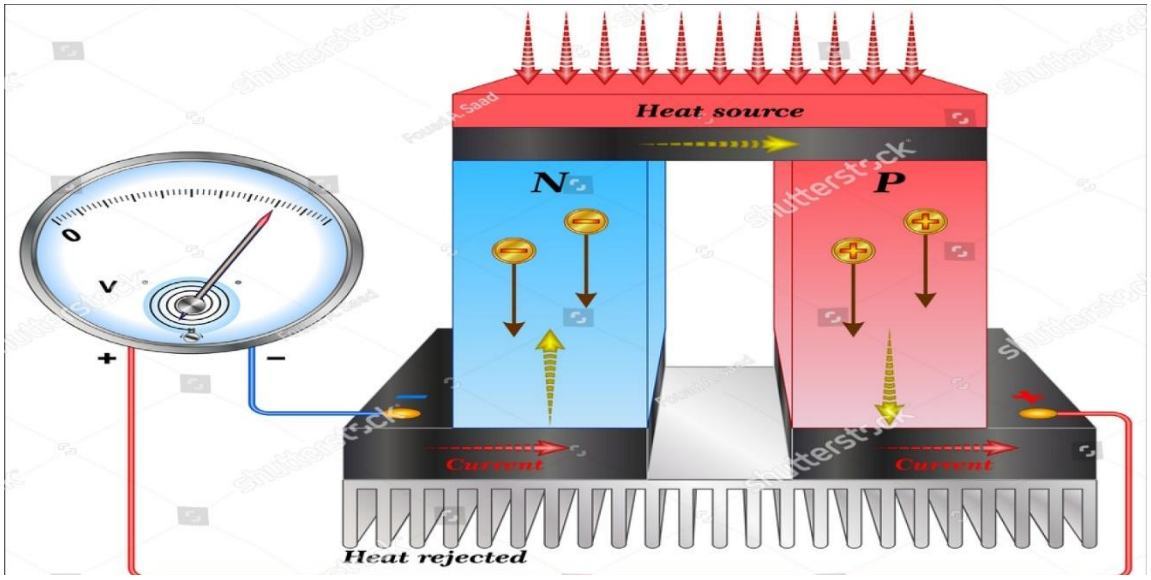

Figure 6: A Seebeck effect is shown by using a thermocouple and multimeter .

The following equation defines the Seebeck coefficient

$$S = - V_{th} / \Delta T \quad \text{.... (1)}$$

The units of Seebeck coefficient, potential difference and temperature are $(\mu V/K)$, V and K respectively [11].

1.4.3. Peltier effect

A process opposite to the Seebeck effect is said to be Peltier effect. In this process the current is passed through the two junctions which results in production of temperature gradient. Peltier in 1834 discovered this effect. When the current is supplied through the two junctions, a thermal flux is created which is given by [12],

$$Q = \pi j \quad \text{.... (2)}$$

where π is the Peltier coefficient.

A thermal barrier impedes heat flow, and the heat absorbed or released at the junctions due to the Peltier effect can be described by the equation:

$$dQ/dt = (\pi_A - \pi_B) \quad \text{.... (3)}$$

and through the junctions π_A and π_B are the Peltier coefficients, V or W/A is the unit of Peltier coefficient [12].

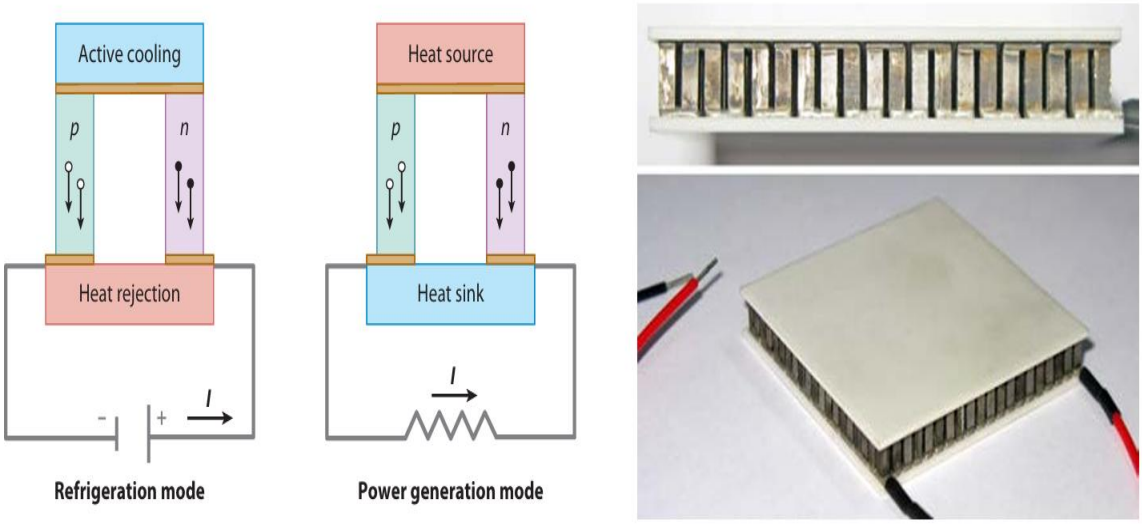

Figure 7: Schematic of a thermoelectric module for refrigeration mode (and called a Peltier cooler) or in power generation mode (and called a thermoelectric generator) [13].

1.5. PROPERTIES OF THERMOELECTRIC MATERIALS

1.5.1. Figure of Merit

Figure of Merit is an important parameter that decides the property of a material to be a good thermoelectric material or not. ZT is the simple denotation and is defined by

$$ZT = \frac{S^2 \sigma T}{k} \quad \text{.... (4)}$$

Now, S is simply the Seebeck coefficient which is having units (V/K).

σ is the electrical conductivity having units (S/m)

k is thermal conductivity having units (W/m-K)

T is measured in kelvin(K) and it is the absolute temperature

To achieve a high figure of merit (ZT), a thermoelectric material must exhibit a large Seebeck coefficient, enabling greater voltage generation from a given temperature gradient. Additionally, it should have high electrical conductivity to facilitate efficient charge transport, and low thermal conductivity to minimize heat loss and maintain the thermal gradient across the material. This combination enhances the overall thermoelectric efficiency. Achieving a good ZT value can enhance thermoelectric technology for waste heat recovery applications, refrigeration and harvestings [12].

1.5.2. Heat transfer

Heat transfer occurs through three primary mechanisms: conduction, convection, and radiation. Among these, thermal conduction refers to the process by which heat energy is transmitted through collisions between neighbouring atoms or molecules in a solid material without any net movement of the material itself. The total thermal conductivity can be divided into two main contributions: k_l from phonons (lattice vibrations) and k_e from electrons. The contribution from magnons, associated with spin waves, is typically negligible and therefore ignored. Hence, the total thermal conductivity is expressed as:

$$\mathbf{k = k_l + k_e} \qquad \text{.... (5)}$$

where k is thermal conductivity. By kinetic theory of gases, k = 1/3 ($C_v$vl), where C_v is the volumetric heat capacity, v is the velocity by which it propagates and l (l = v × T) is the mean free path is l (l = v × T) and the relaxation time is T.

The second one term of thermal conductivity that is due to electrons, will give us a result

$$\mathbf{k_e = \frac{\pi^2 n K_B^2 T \tau}{3 m_e}} \qquad \text{.... (6)}$$

then after rearranging

$$\mathbf{k_e = \frac{\pi^2}{3}\left(\frac{k_B}{e}\right)^2 \sigma T} \quad \text{.... (7)}$$

and

$$\mathbf{k_e = L_0 \sigma T} \quad \text{.... (8)}$$

This is also known as Wiedemann Franz law which provides a relation between electronic thermal conductivity and electrical conductivity through the absolute temperature, where L_0 is the Lorentz number having value $L_0 = 2.44\times10^{-8}$ $W\Omega k^{-2}$ [12].

1.5.3. Electrical transport

By Boltzmann transport theory, the electrical conductivity is

$$\mathbf{\frac{1}{\rho} = \sigma = ne\mu} \quad \text{.... (9)}$$

where n is the charge career concentration, μ is the mobility and e is the elementary charge [12]. And another relation,

$$\mathbf{\mu = \frac{e\tau}{m^*}} \quad \text{.... (10)}$$

Where average time between collisions is τ is the and effective mass is m^*.

The sign of the Seebeck coefficient reflects the type of majority charge carriers in a material. A positive Seebeck coefficient indicates that holes are the dominant carriers, while a negative value signifies that electrons are the majority charge carriers.

When multiple conduction pathways are involved, the overall Seebeck coefficient is calculated as the weighted average of the individual contributions from each channel. Therefore,

$$\mathbf{S = \frac{S_1\sigma_1 + S_2\sigma_2}{\sigma_1 + \sigma_2}} \quad \text{.... (11)}$$

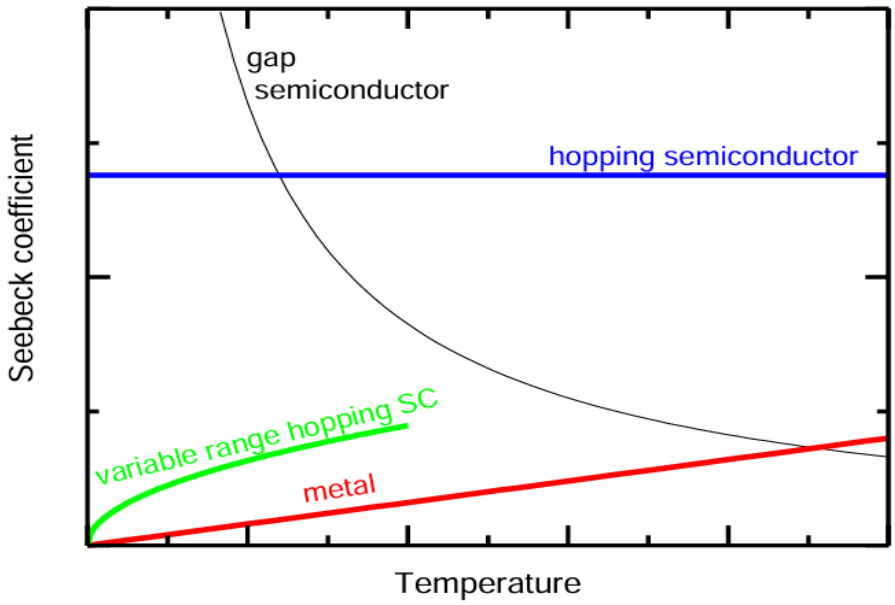

Figure 8: Schematic of Seebeck coefficients Vs Temperature of metal and semiconductor [12].

1.6. METAL CHALCOGENIDES BASED GAS SENSORS

In essence, metal chalcogenide gas sensors are a subset of metal selenide-based gas sensors. The transfer of charges to or from the sensing material to the specific target gas is the basic mechanism. There are two different kinds of gases: reducing and oxidizing.

Oxidizing gases are those that draw electrons away from detecting materials due to their higher electron affinity, while reducing gases are those that give electrons to the sensing material.

Let us understand by simple example of the target oxidizing gases NO_2 and O_2 [14].

$$O_2\,(gas) + e^- \longrightarrow O_2^-\,(adsorbed)$$

$$NO_2(gas) + e^- \longrightarrow NO_2^-(adsorbed)$$

$$NO_2(gas) + O_2^-\,(ads.) + 2\,e^- \longrightarrow NO_2^-(ads.) + 2O_2^-(ads.)$$

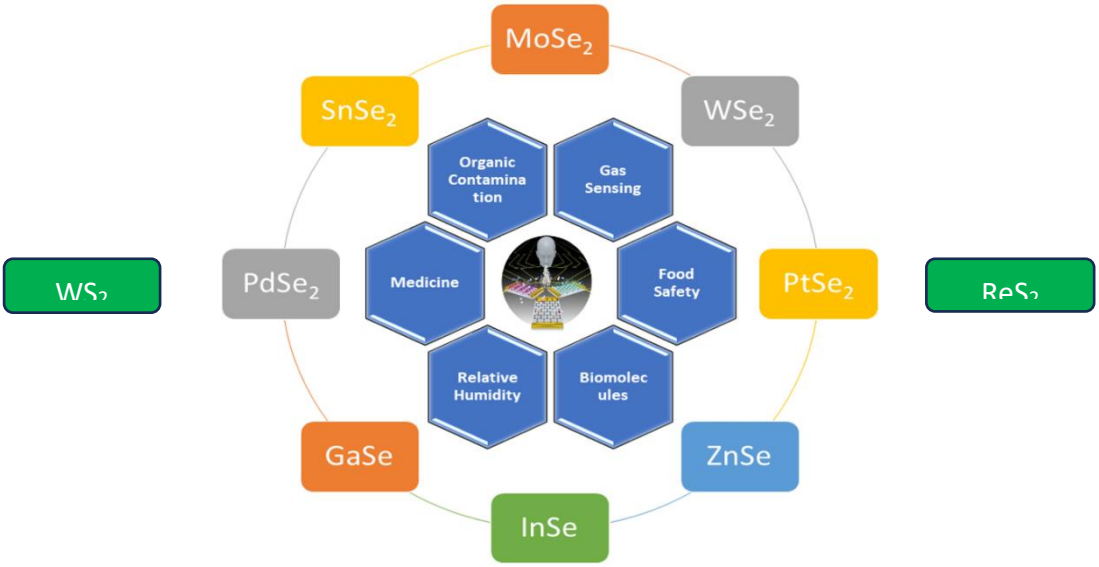

Figure 9: Various applications of metal selenides and sulphides.

The many kinds of metal chalcogenides or dichalcogenides gas sensors are depicted in figure 9. These metal chalcogenides also have several uses in a variety of industries, including organic pollution, food safety, and medicine [14-16].

1.7. SnSe THIN FILM GAS SENSOR AND THERMOELECTRIC MATERIAL

SnSe is a good gas sensing material to sense NO_2, NH_3 and CH_4 type gases due to the suitable narrow band gap generally ranges from 0.9 – 1.3 eV and low thermal conductivity < 0.4 $Wm^{-1}K^{-1}$, high surface energy that leads the interaction between the sensing material and the target gases and having high surface to volume ratio as observed from the surface morphology. Our analysis also showed that SnSe is a more cost-effective material compared to other metal oxide semiconductors and metal chalcogenide gas sensors [17].

Thermoelectric property of this material also showed good results of 2.6 ZT [18,19] figure of merit. The high ZT value indicates that the material is an effective thermoelectric generator. The main advantage of SnSe as a gas sensor is that it is highly selective to particular gas and its operating temperature is also low.

CHAPTER 2: LITERATURE REVIEW

2.1. Synthesis, characterization and properties of SnSe thin films

S Rani *et al.* [19] employed the thermal evaporation method to deposit SnSe thin films onto soda-lime glass substrates. The optimized film thickness was 843 nm, achieved by applying a low-tension current of 90 A and a voltage of 20 V for a duration of at least 2 minutes. High-purity SnSe powder with a stoichiometric ratio of 1:1 was used as the source material. Comprehensive characterization techniques were conducted, including X-ray diffraction (XRD), scanning electron microscopy (SEM), and UV-Vis-NIR spectroscopy. XRD analysis confirmed the formation of single-phase SnSe, while UV-Vis-NIR spectroscopy revealed a direct band gap of 1.3 eV. SEM imaging indicated a nanostructured surface morphology. Finally, the SnSe thin film was evaluated for gas sensing performance and demonstrated effective sensitivity toward NO_2, confirming its potential as a promising gas sensing material.

W Yang *et al.* [20] synthesized SnSe thin films on glass substrates using the thermal evaporation technique. The process utilized high-purity (99.999%) SnSe powder with a 1:1 stoichiometric ratio. During deposition, the source temperature was maintained at 450 °C under a vacuum pressure of 5×10^{-4} Pa. A range of characterization methods was applied to analyse the structural and chemical properties of the films. X-ray diffraction (XRD) confirmed the presence of a single-phase structure. The film's surface morphology and elemental composition were assessed using field emission scanning electron microscopy (FE-SEM) along with energy-dispersive X-ray spectroscopy (EDX). Crystalline features were validated through field emission transmission techniques, while transmission electron microscopy (TEM), X-ray photoelectron spectroscopy (XPS), and Raman spectroscopy provided additional insights into the film's microstructure and bonding states. Finally, the SnSe films were tested for their gas sensing capabilities, showing strong responsiveness to low concentrations of NO_2 at ambient temperature.

M Kumar *et al.* [21] employed a one-step thermal evaporation method to deposit SnSe thin films using high-purity SnSe powder with a 1:1 stoichiometric ratio. The deposition was carried out under a vacuum pressure of 8×10^{-6} Torr, applying a low-tension current of 100 A and a voltage of 20 V. The structural properties of the films were

analysed using X-ray diffraction (XRD), while UV-Vis-NIR spectroscopy revealed a direct band gap of 1.18 eV. Raman spectroscopy was also performed, and the surface morphology was examined through scanning electron microscopy (SEM). Subsequent measurements confirmed that the SnSe thin film functions as a UV-Vis photodetector; however, its responsivity was relatively low. The study suggested that performance could be improved through alternative approaches such as heterostructure formation or doping.

Weiran Shi *et al.* [17] explored various methods to deposit SnSe films, including solution-based techniques and vapor phase methods such as Physical Vapor Deposition (PVD) and Chemical Vapor Deposition (CVD). The films were studied for their thermoelectric and electrical properties. Additionally, doping with elements like Ag, I, $BiCl_3$, Tl, Cu, and Zn was investigated to enhance these properties. The SnSe films exhibited an orthorhombic crystal structure, with optical band gaps measured as 0.9 eV (indirect) and 1.3 eV (direct). It was noted that the band gap values depend on the deposition technique used. SnSe thin films have been applied in various technologies, including phase change memory devices, sodium- and lithium-ion batteries, and topological insulators. Furthermore, SnSe demonstrated a high thermoelectric figure of merit (ZT) of 2.6 at 923 K.

D Alagarasan *et al.* [22] fabricated SnSe thin films using thermal evaporation of 99.999% pure SnSe powder under high vacuum conditions at a pressure of approximately 10^{-6} Torr. The films were deposited on bare glass substrates positioned 15 cm from the source, achieving an optimized thickness of 600 nm at a deposition rate of 2 Å/s. X-ray diffraction (XRD) analysis confirmed the SnSe phase, while scanning electron microscopy coupled with energy-dispersive X-ray spectroscopy (SEM-EDX) was used to examine the film's morphology and composition. The lattice parameters were determined as a = 11.25 Å, b = 4.13 Å, and c = 4.48 Å, indicating an orthorhombic crystal structure. Raman spectroscopy detected minor traces of $SnSe_2$. The surface morphology was nanostructured, and UV-Vis NIR spectroscopy revealed that the direct band gap varied between 0.87 and 1.13 eV, depending on the substrate temperature during deposition. Electrical measurements showed that increasing annealing temperature enhanced the photocurrent response. These results demonstrate that SnSe thin films exhibit promising photodetector performance with high response speeds.

H Yanuar *et al.* [23] fabricated SnSe films using the close spaced vapor transport (CSVT) technique on SnO_2-coated soda-lime glass substrates. The films deposited at a source temperature of 650 °C and a substrate temperature of 600 °C exhibited optimal properties. Structural analysis by X-ray diffraction (XRD) confirmed the film's crystallinity, while scanning electron microscopy with energy-dispersive X-ray spectroscopy (SEM-EDX) provided insights into the morphology and composition. The indirect band gap was determined to be 0.916 eV. Electrical characterization using four-probe Hall measurements showed that the films exhibit *p*-type conductivity, with a resistivity of 17 Ω-cm, hole concentration of 4.7×10^{18} cm^{-3}, and carrier mobility of 1.56 $cm^2 \cdot V^{-1} \cdot s^{-1}$.

G. Jeong *et al.* [24] fabricated single-phase SnSe thin films using the thermal co-evaporation method with a selenium thermal cracker. The Sn to Se composition ratio varied between 1:1 and 0.95:0.99. Depositions were carried out at a substrate temperature of 100 °C and a vacuum pressure near 10^{-6} Torr, while the thermal cracker was maintained at 800 °C. The films' structural, morphological, and compositional characteristics were examined using X-ray diffraction (XRD) and scanning electron microscopy coupled with energy-dispersive X-ray spectroscopy (SEM-EDX). Electrical properties including carrier density, mobility, resistivity, and conductivity were evaluated as a function of stoichiometric variation. Additionally, the influence of dopants antimony (Sb) and indium (In) on the electrical behaviour of SnSe films was investigated.

CHAPTER 3: EXPERIMENTAL WORK

3.1. THERMAL EVAPORATION METHOD

There are two most used techniques of thin film deposition that are

(i) CVD (Chemical Vapour Deposition)

(ii) PVD (Physical Vapour Deposition)

Thermal evaporation is a type of Physical Vapor Deposition (PVD) technique. In this process, the source material, placed in a boat or crucible, is heated resistively until it vaporizes. Usually, the crucible is made of Molybdenum which have a high melting point, thermally stable, chemically and thermally inert with the source material. After the melting point the source material melts and evaporates and then goes to the desired substrate and deposits on the substrate as a film. Substrate may be a glass or any other material which have a high melting point and chemically inert with the source material. The entire thermal evaporation process takes place inside a vacuum chamber, often called a bell jar. The pressure is reduced to around 10^{-6} Torr to minimize contamination during the material deposition and also provides a clean environment for deposition and increase the mean free path of the source molecule which is evaporated [25].

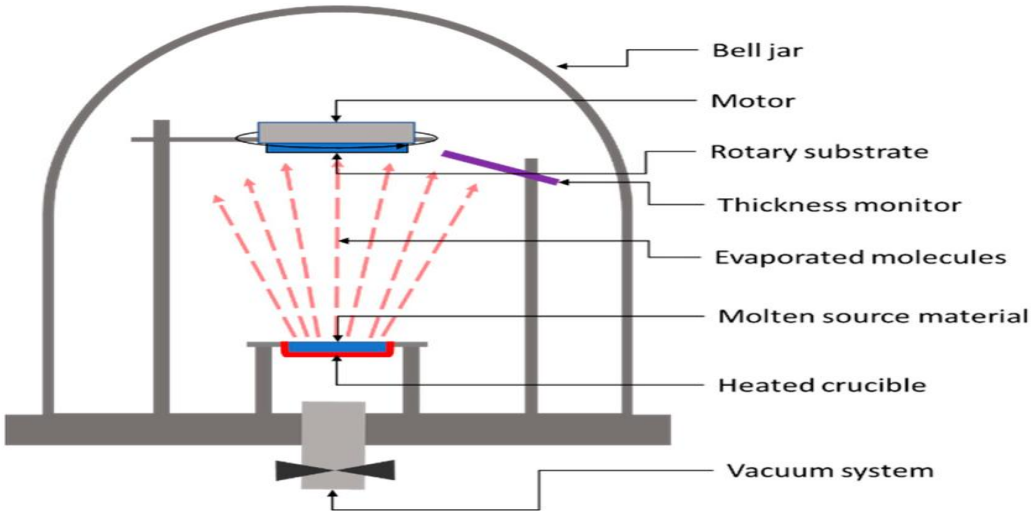

Figure 10: Schematic of thermal evaporator system.

3.2. COMPONENTS OF THERMAL EVAPORATION SYSTEM

3.2.1. Vacuum coating unit

For less contamination of the deposited material, the source material has to be in the clean environment in a high vacuum chamber by creating a pressure of roughly around 10^{-6} Torr which increases the mean free path of the source molecules.

3.2.1.1. Rotary Pump

The working principle of the Rotary pump is Boyle's law. Boyle's law gives a relation between pressure and volume

$$P_1V_1 = P_2V_2 \quad \text{.... (12)}$$

Sliding vanes are connected to a rotor and are spring-loaded between their initial and end positions, allowing them to expand or contract as needed. Oil is used to create a seal, preventing gas molecules from leaking through the ends of the vanes, and also helps transfer heat to the chamber walls. As the rotor turns in one direction, the vanes sweep the molecules inside the chamber and expel them through the exhaust outlet. The whole rotary pump is connected to the vacuum gas chamber by gas ballast inlet value [26].

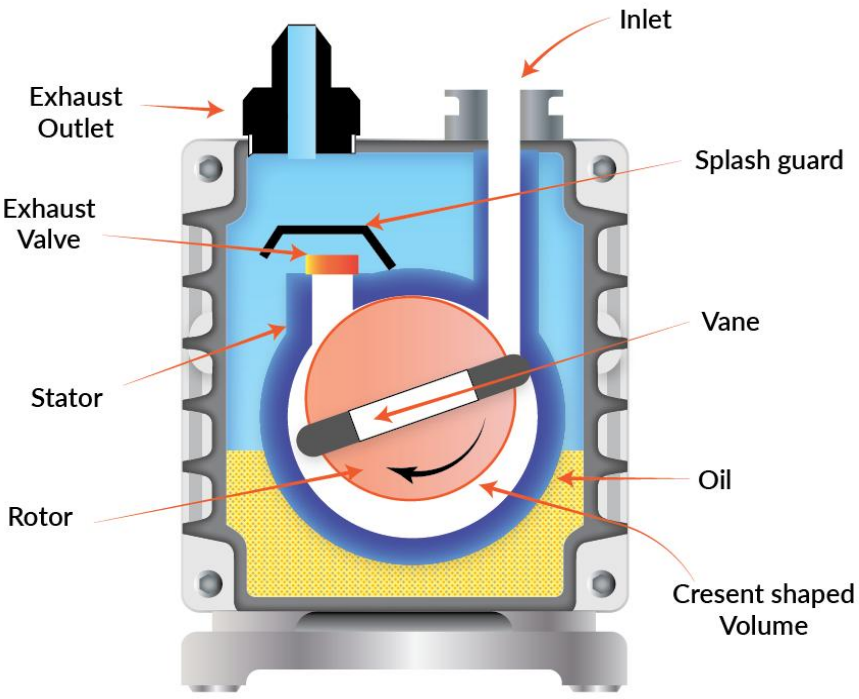

Figure 11: Schematic of Rotary pump.

3.2.1.2. Diffusion Pump

The diffusion pump operates based on the principle of momentum transfer. A specialized oil is placed at the bottom of the pump and heated for about 10 minutes until it vaporizes. The rising vapor captures gas molecules from the chamber above and carries them toward the pump's compression stages. Due to the oil's higher density, it condenses and flows back to the bottom, while the entrained gas molecules are expelled through successive compression stages. The diffusion pump is typically connected to a backing pump and then to the vacuum chamber, enabling the system to achieve high vacuum levels, typically around 10^{-6} Torr [26].

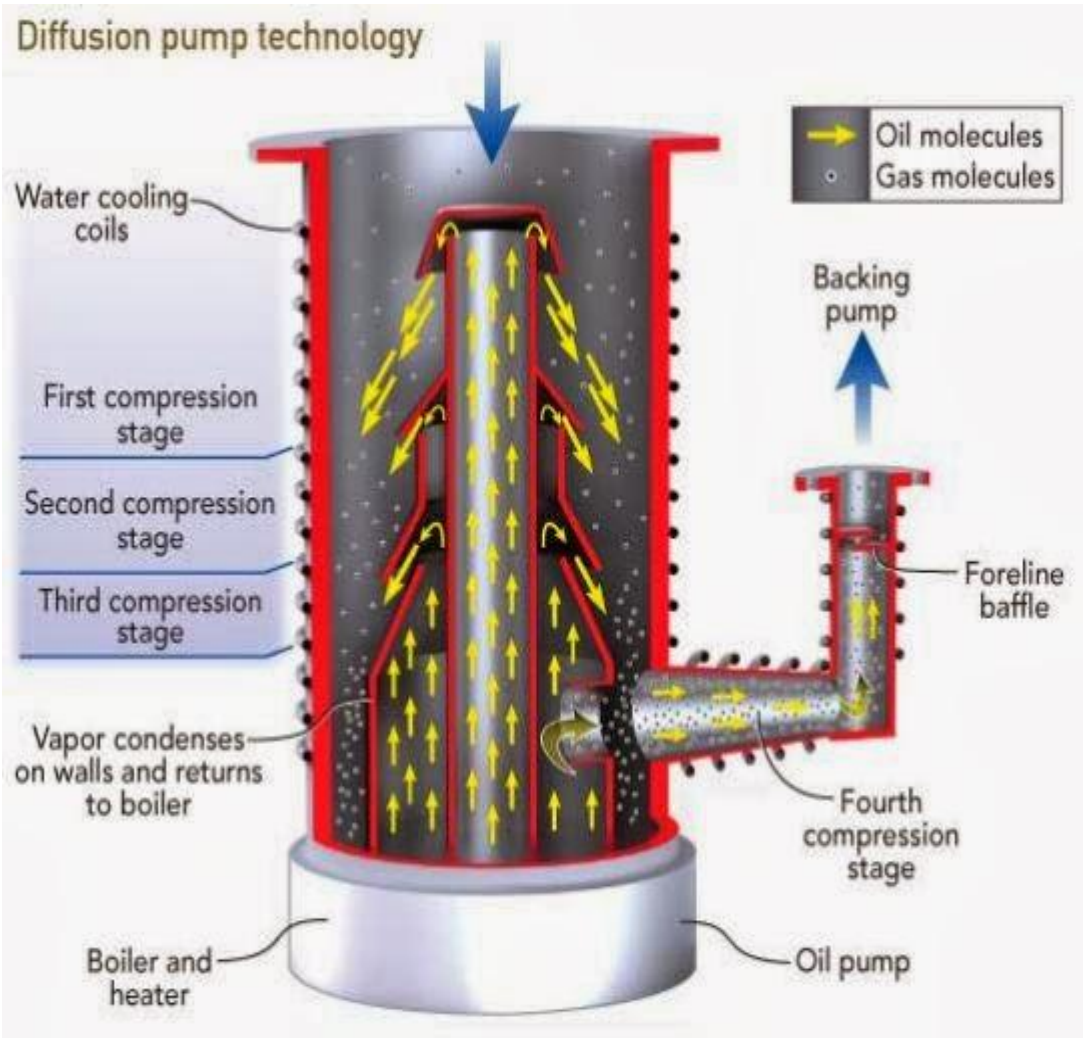

Figure 12: Schematic of Diffusion Pump.

3.3.1.3. Pirani Gauge

Pirani gauge is based on the principle of Wheatstone Bridge set up, where four resistors are in the form of a bridge and the three resistors are known and one is unknown. Unknown resistor can be measured by balancing the condition. In this case, the unknown resistor is Pirani gauge filament [24].

Where $R_1/R_2 = R_3/R_4$ and $R_P = (R_3 \times R_2)/ R_4$

Where R_P is the Pirani resistor and now by calibration, conversion of resistance into equivalent pressure value can be easily done.

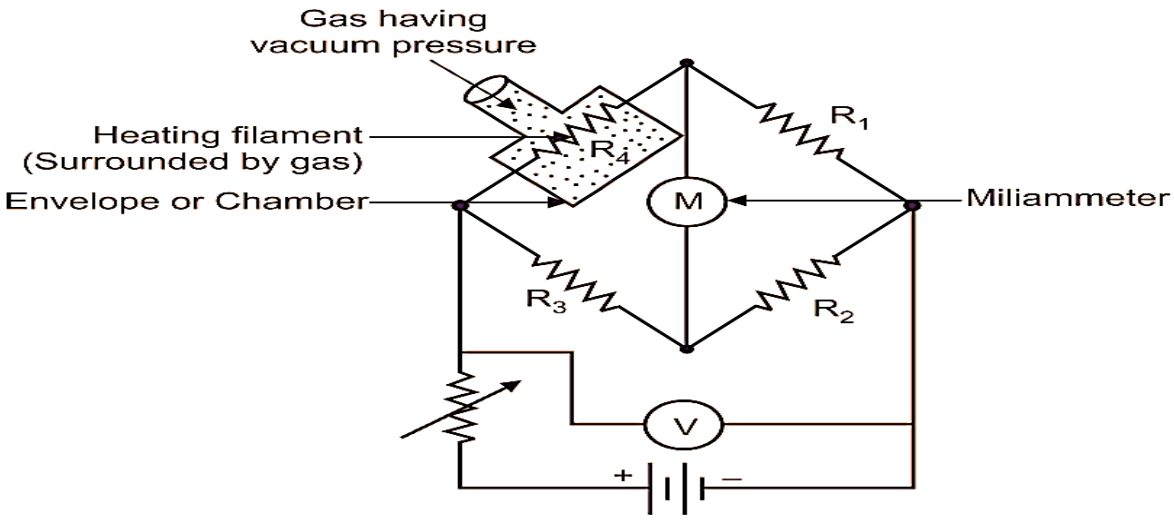

Figure 13: Schematic of Pirani Gauge by Wheatstone bridge setup.

3.3.1.4. Penning Gauge

Penning Gauge comes under the ionization gauge. Two cathodes are placed parallelly and one anode in the centre is placed parallel to the two cathodes. Potential of about 2 kV is applied between cathode and anode and about 400 G of magnetic field is applied perpendicular to the electrodes. The emitted electron follows the helical path in between two cathodes and even low pressure can be sensed easily by ionization [26].

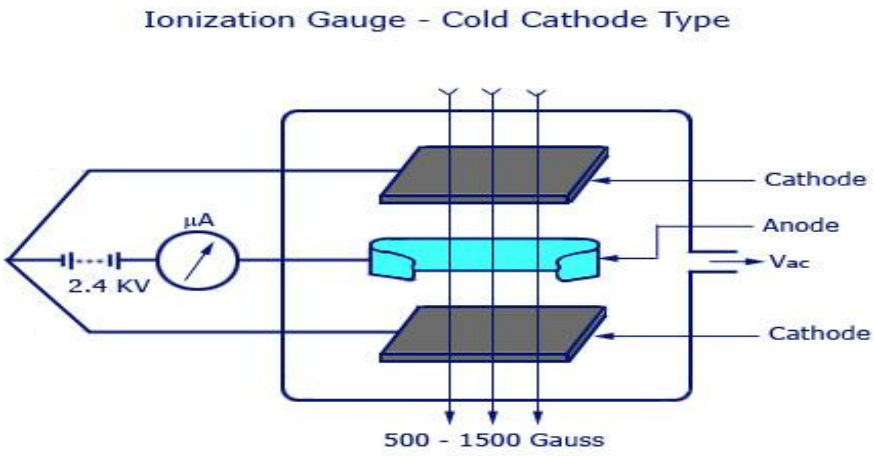

Figure 14: Schematic of Penning Gauge.

3.2.2. Resistive heater

The basic working principle of resistive heating is based on Joule's heating phenomenon, by a relation

$$H = I^2RT \quad \text{…. (13)}$$

The boat or crucible glows when one passes the current through it. Due to high resistance of the boat, the electrical energy converted into the heat energy. The source material for evaporation is placed inside this boat. The boats are made up of metals which are having a higher melting point like Tungsten, Molybdenum and are chemically and thermodynamically inert in nature.

3.2.3. Quartz Thickness Monitor (QTM)

QTM is used to estimate the thickness and deposition rate of the thin film during deposition process. It is installed inside the vacuum chamber near the substrate holder. When a thin film is deposited onto the surface of the crystal, its mass increases, leading to a corresponding decrease in the oscillation frequency. This change in frequency is used to measure thickness of the deposited film with high precision.

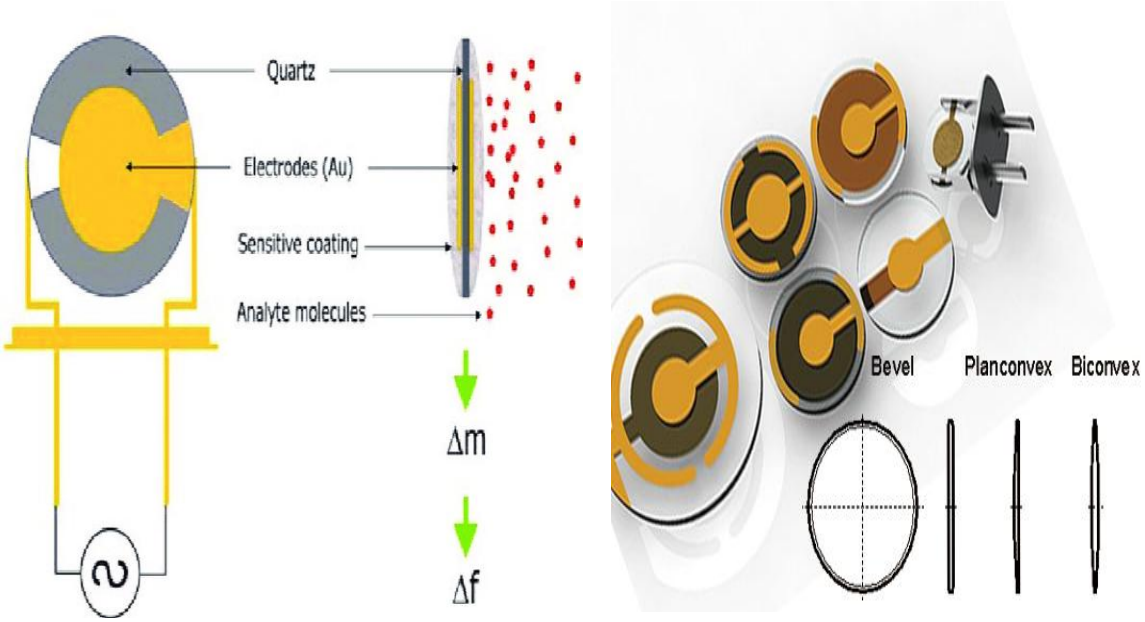

Figure 15: Quartz crystal and its connections for thickness monitor.

3.2.4. Substrate Holder

The substrate holder is located at the top inside the vacuum chamber. It is positioned directly above and perpendicular to the source boat. The holder is designed to accommodate up to three substrates, allowing for easy loading and uniform film deposition.

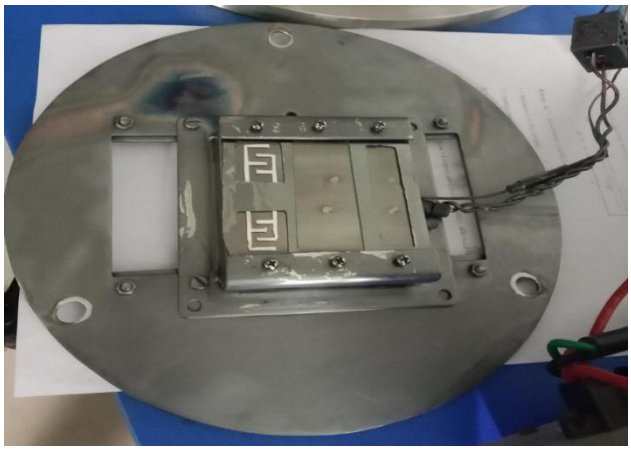

Figure 16: Three Substrates loaded in substrate holder with mica mask on the substrates for pattering.

3.2.5. Shutter

A shutter acts like a gate for thin film deposition. It is commonly used to control the precise thickness of the film by temporarily blocking the source material from reaching the

substrate. When the shutter is closed, no film is deposited on the substrate. This feature is especially useful when the current or heating of the filament is difficult to control accurately, allowing better regulation of the film thickness.

3.2.6. Gas mass flower

An inert atmosphere can also be created by introducing gas through a mass flow controller connected to a valve on the vacuum chamber.

3.2.7. Water cooling system

To prevent unwanted heat that could contaminate the substrate, a water-cooling system is installed around the vacuum chamber. This system uses cooled water to reduce overheating of both the substrate and the chamber. By maintaining a lower temperature, the water-cooling system minimizes the evaporation of impurities inside the chamber, thereby reducing the risk of contamination during thin film deposition.

3.3. DEPOSITION OF SnSe THIN FILMS

3.3.1. Substrate cleaning process

- ✓ Chose the glass substrate with no scratches.
- ✓ Clean the substrate using soapy water, followed by rinsing with distilled water.
- ✓ Perform ultrasonication for at least three cycles, each lasting approximately 5 minutes.
- ✓ After that, clean the substrate with boiling ethanol.
- ✓ Finally, carefully load the cleaned substrates into the substrate holder.

3.3.2. Tooling factor

Tooling factor is the ratio of the square of the distance between source material to the quartz crystal and source to the substrate. The formula for tooling factor is given below

$$\text{Tooling factor} = (D^2/S^2) \times 100$$

Where distance from crystal to source is denoted by D and the distance from substrate to source is S.

3.3.3. Variation in Substrate temperature

SnSe thin film were deposited by using thermal evaporation technique by altering the substrate temperature from room temperature to 200 ˚C. First, the Silver (Ag) finger like electrode were deposited by using the mica masks on the substrates at 200 ˚C of substrate temperature.

Table 3: Parameters for deposited Ag electrodes.

Material	Current (A)	Pressure (mbar)	Rate (Å/s)	Thickness (Å)
Ag	7.85, 148	1.5×10^{5}	2	2500
Ag	7.35, 156	1.2×10^{5}	2	2500

Tooling factor = 87.422 and Substrate temperature = 200 ˚C

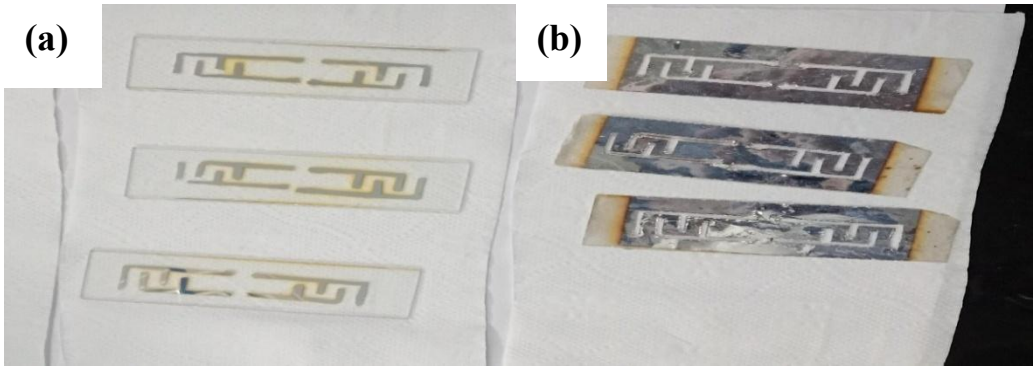

Figure 17: (a) Ag finger type electrodes (b) mica mask pattern.

Table 4: Parameters for SnSe thin film deposited on the glass substrate using SnSe powder.

Current (A)	Pressure (mbar)	Rate (Å/s)	Thickness (Å)	Tooling factor	Substrate temperature
4.75 (P) 96 (S)	4.75×10^{-6}	2	6000	84.64	RT
4.4 (P) 90 (S)	4.5×10^{-6}	2.5	6000	83.35	100 ˚C

4.4 (P) 90 (S)	5.4×10^{-6}	2.5	6000	73.82	150 ˚C
4.85 (P) 98 (S)	7×10^{-6}	2	6000	87.422	200 ˚C

Where ‘P’ and ‘S’ are the primary and secondary currents respectively.

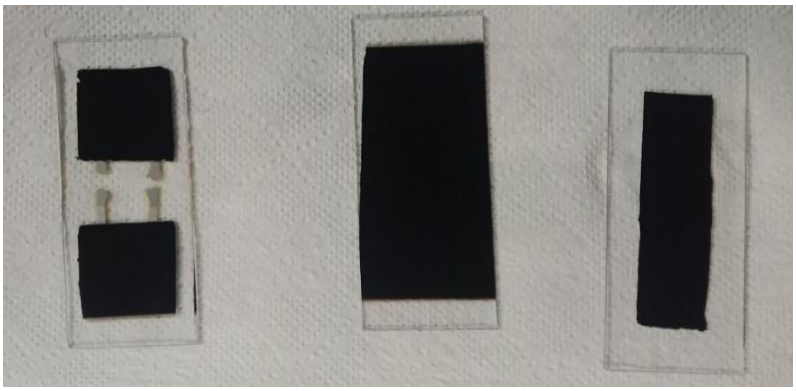

Figure 18: SnSe deposited for gas sensing device with silver electrodes, for characterization and for Thermoelectric properties respectively.

Figure 19: Thermal Evaporation Machine.

CHAPTER 4: CHARACTERIZATION TECHNIQUES

4.1. XRD (X - Ray Diffraction)

X Ray Diffraction technique reveals about the crystal structure. X-Rays are diffracted or reflected by the crystal atoms which are placed on the basis. It can identify whether the sample is crystalline, polycrystalline or amorphous. It also provides information about stress or strain present in the sample by using W-H plot method. XRD is also known as the fingerprint technique to identify the sample. The X-rays used are characteristic X-rays, typically with K_β radiation suppressed using a K_β filter. The necessary condition for the diffraction of the X-rays is that X-rays wavelength must be comparable to the interatomic spacing of crystal planes [27].

Bragg's Law- Bragg's gives a relationship between the angle at which X-rays produced a highly intense sharp peak and the interplanar spacing 'd'. The geometry for the Bragg's law is shown in figure 20.

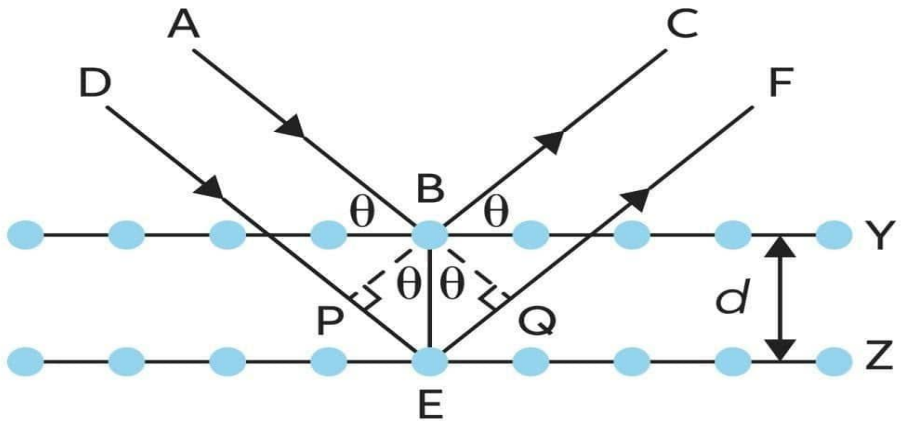

Figure 20: Geometry for XRD.

Consider the two incident X-ray beams AB and DE that incident at angle θ with the crystal planes and BC and EF are the two diffracted beams with the same angle. To find the path difference between these two parallel X-ray beams, the normal is drawn from point B on DE and EF. In ΔBPE and ΔBQE, the total path difference is PE+EQ, therefore

$$\Delta = PE + EQ$$

By using trigonometry,

PE = EQ = dsinθ, therefore

Therefore, path difference = dsinθ + dsinθ = 2 dsinθ

The criteria for the constructive interference of the two parallel X-rays is that they must be in same phase

$$\mathbf{2dsin\theta = n\lambda} \qquad \textbf{…. (14)}$$

where, d – interplanar spacing

λ – wavelength of X- ray

n – order of diffraction

This equation (15) gives the estimation of various parameters of the crystal.

$$\mathbf{d} = \frac{\mathbf{1}}{\sqrt{\frac{h^2}{a^2}+\frac{k^2}{b^2}+\frac{l^2}{c^2}}} \qquad \textbf{…. (15)}$$

Lattice parameters can be easily found if the interplanar spacing is known, where h, k and l are the Miller indices and a, b, and c are lattice parameters of the crystals [28].

Debye – Scherrer's formula – By using the Debye – Scherrer's formula, the crystallite size can be determined. Formula is given below –

$$\mathbf{D} = \frac{k\lambda}{\beta \cos\theta} \qquad \textbf{…. (16)}$$

where, λ – wavelength of X- ray

k – Scherrer constant

D – Average crystallite size of the crystal

β – Full wavelength of half maxima

Working of X-Ray Diffractometer – There are three major components of X-ray diffractometer **(i) X-Ray source, (ii) X-Ray detector** and the **(iii) sample holder.**

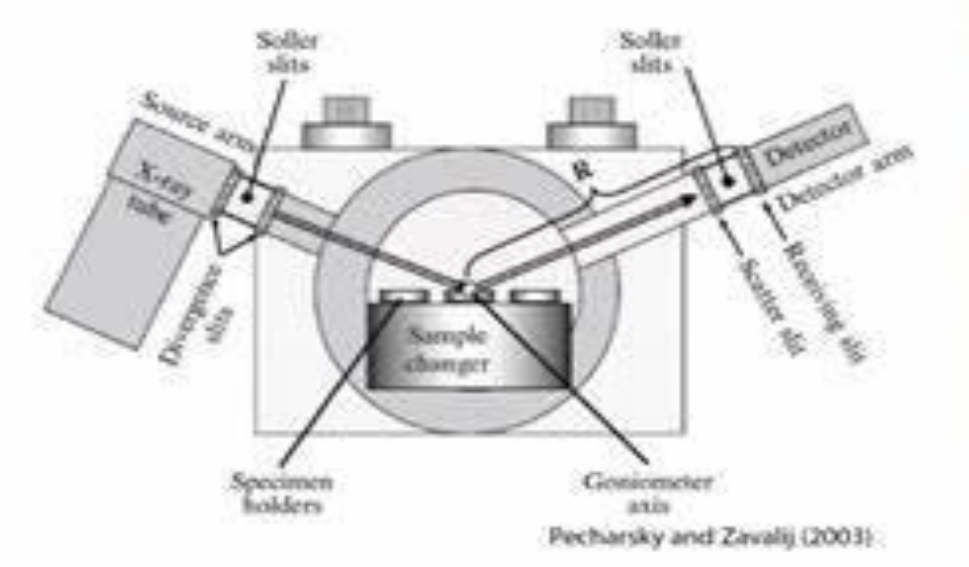

Figure 21: Schematic of XRD.

When the X-Rays from the source illuminate the sample, crystal atoms diffract the X-rays and direct towards the detector. By adjusting the positions of the detector and the sample, the diffraction angle 2θ changes. At specific 2θ values, intense peaks appear, corresponding to constructive interference from certain crystal planes. The angle between the incident and diffracted X-rays is θ. By varying the incident angle and adjusting the sample position, the crystal structure can be thoroughly analysed [27].

Figure 22: X- Ray Diffractometer Instrument.

4.2. RAMAN SPECTROSCOPY

Raman Spectroscopy serves as a complementary technique to XRD, helping to confirm the material's properties. In Raman Spectroscopy, the sample is first illuminated with monochromatic light, typically from a laser. The scattered light from the sample is then analysed using a spectrometer. When the sample absorbs the light energy, electrons are excited to higher energy states and subsequently return to vibrational energy levels of the ground state, emitting scattered light.

There are three types of scattered light lines observed:

- The **Rayleigh line**, where the scattered light has the same frequency as the incident light (no change in energy).
- The **Anti-Stokes line**, where the scattered light has a slightly higher frequency than the incident light (energy gain).
- The **Stokes line**, where the scattered light has a lower frequency than the incident light (energy loss).

The shifts in frequency occur due to the vibrational energy levels of the molecules in the sample, providing insight into the material's molecular structure.

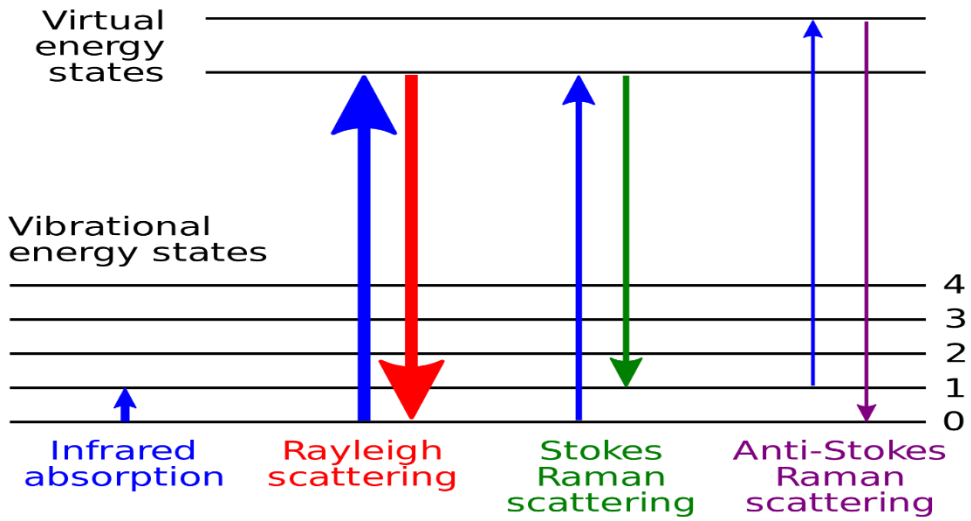

Figure 23: Various vibrational states and different scatterings.

The necessary criteria for a material to show the Raman spectra is that it should have the polarizability present in that molecule; no dipole moment is required for Raman spectra. There are various components for Raman spectra. The Raman spectra provide an information about chemical bonding and vibrational modes [27].

Excitation Laser – It excites the electrons to the higher energy level by incidenting the photon, generally used the monochromatic coherent laser sources. Then after passing through the different filters, light is reflected from the mirror then focused by the focusing lens on the sample.

Wavelength Selector – The different filters decide a single wavelength laser that incidents on the sample so that it excites the electrons to that particular specified energy level.

Detector – Detector may be photomultiplier tubes or photodiode arrays to detect the deexcited photon of particular frequency.

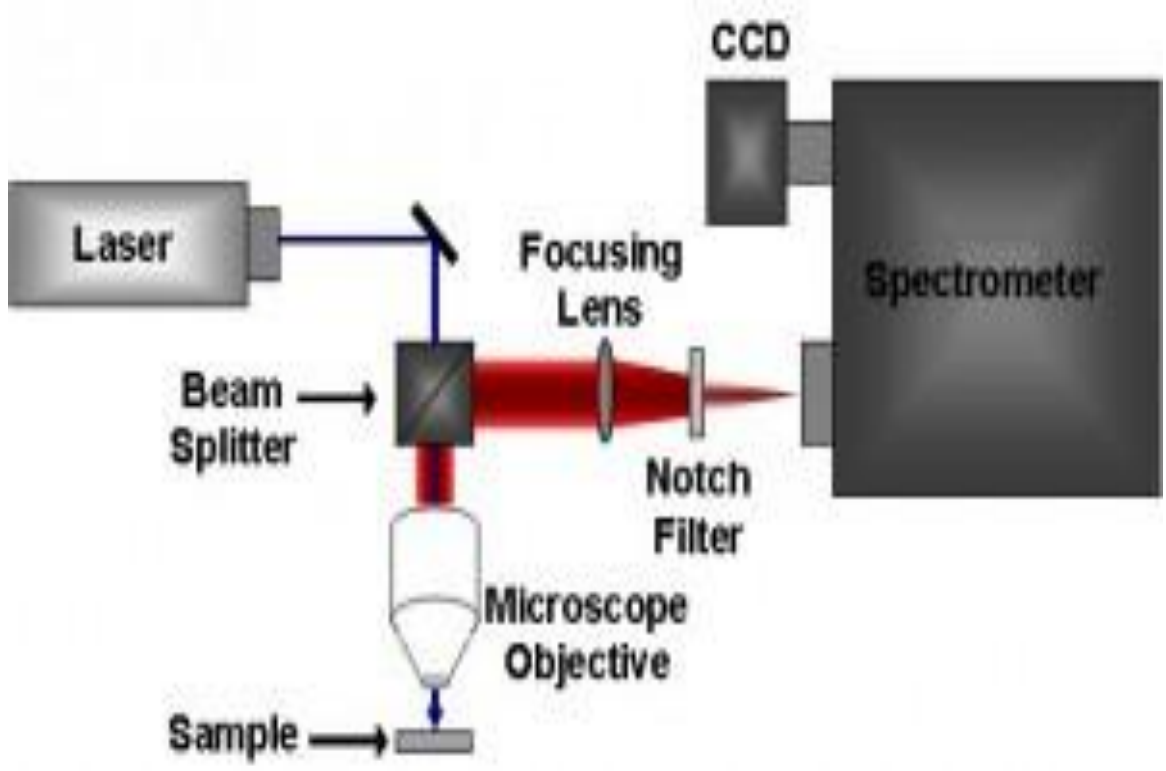

Figure 24: Schematic of Raman spectrophotometer.

4.3. FESEM – EDX (Scanning Electron Microscope and Energy Dispersive X-Ray Spectroscopy)

4.3.1. SEM (Scanning Electron Microscope)

The SEM provides an information about the surface morphology of the sample.

Components of SEM

Electron Source – The electron source is generally made from W(Tungsten) filament. It is essential to prevent oxidation of the filament to maintain its functionality. To minimize electron scattering during operation, a high vacuum environment is required.

Electromagnetic lenses – These lenses are used to focus the electron beams and also to demagnify the electron beam as the electron probe.

Deflection System – This is used to scan the sample by providing the specific voltage to the EM lenses.

Electron detector – Detector is used to detect secondary and backscattered electrons

The whole set up is connected to the data acquisition unit to a computer.

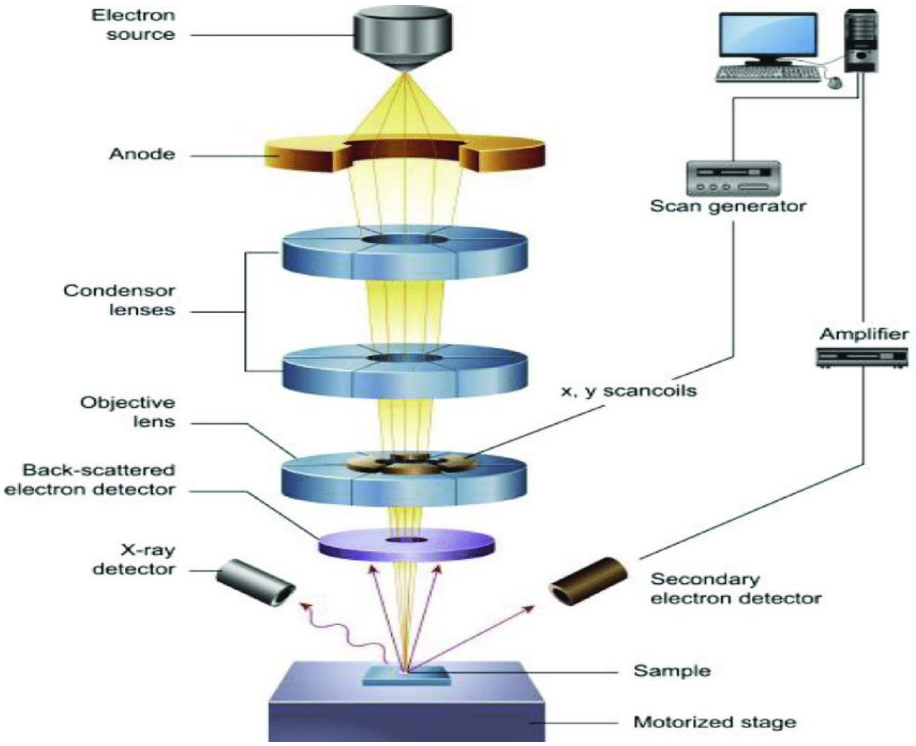

Figure 25: Schematic of SEM.

Working

- Electron gun generates the electrons by thermionic emission or by applying electric field; to reduce the potential barrier and work function generally the electric field is applied with intensity 10 Vnm^{-1} so that metal can eject the electrons from its surface.
- To focus the electron beam there are EM lenses, they compress the spot size and focus with minimum diameter of the beam. SEM is having a 10 nm spot size and 1 μm penetration depth.
- By using the scanning coils, the electron beam as a probe can move throughout the sample in the straight line by doing rectangular raster scan. For enlarged view of the image the probe area should be minimized by increasing the voltage of the EM lenses. Working distance and the distance to the specimen from the last lens plays a crucial role for the pixels to show the better resolution.
- SEM creates secondary electrons as well as backscattered electrons that can be detected by the different detectors. By applying positive voltage in PMT, it detects the backscattered electrons and if it is negative voltage, it detects both backscattered and secondary electrons.
- SEM can provide a magnification of about 10 to 50 kX.
- When a three-dimensional image is generated using a Scanning Electron Microscope (SEM), it allows for detailed analysis of the surface topography of the sample. From the secondary electrons estimation of the surface texture can be easily done and by backscattered electrons one can examine the topography contrast [27].

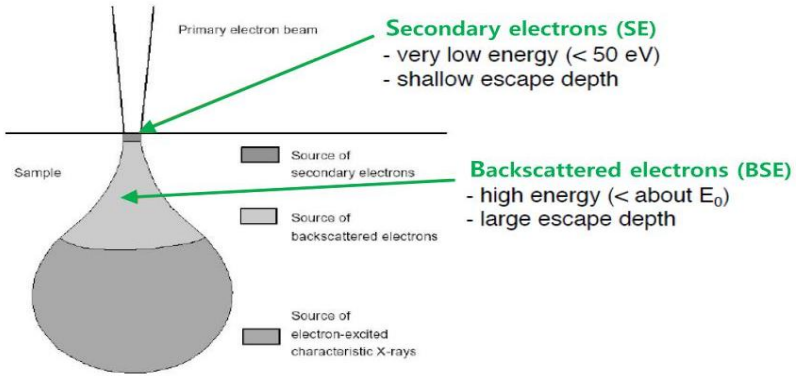

Figure 26: Different types of electrons ejected by SEM.

4.3.2. EDX (Energy Dispersive X-Ray spectroscopy)

X-rays are produced when high-energy electrons emitted from an electron gun strike the surface of a target material. Upon impact, these electrons rapidly decelerate and lose their kinetic energy, which is then converted into electromagnetic radiation in the form of X-rays. This sudden deceleration results in the emission of photons, commonly referred to as characteristic X-rays, which are widely used for both qualitative and quantitative analysis of materials [27].

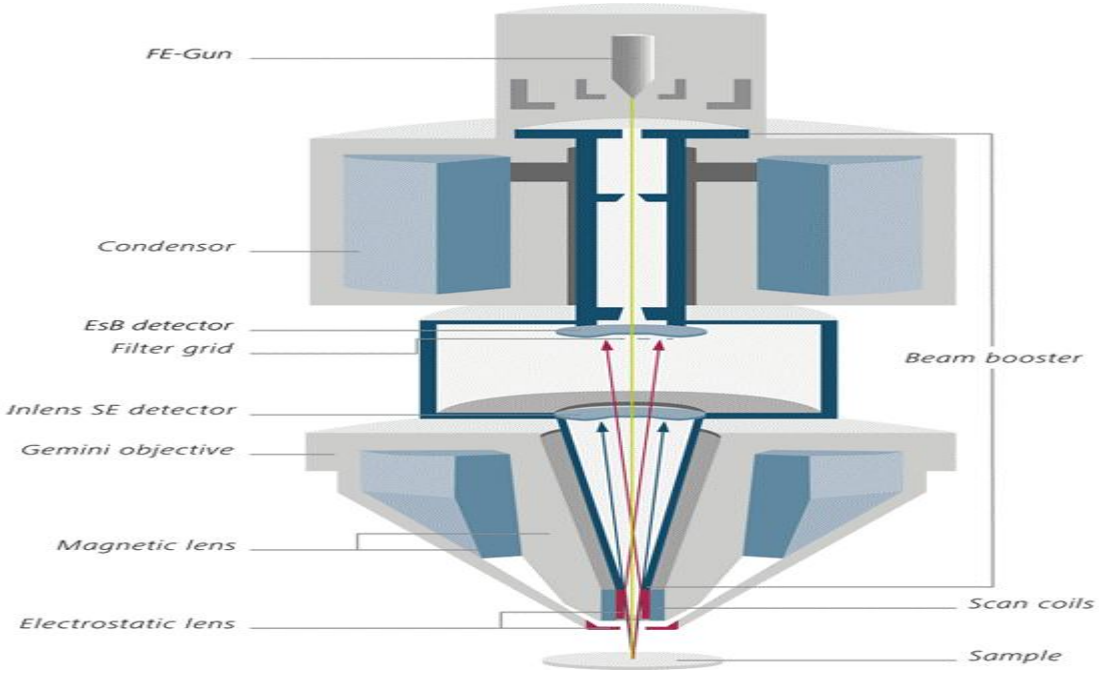

Figure 27: Schematic of EDX attached with SEM.

4.4. UV-Vis NIR Spectroscopy

By using the UV-Vis NIR spectroscopy, the transmittance and reflectance of the prepared material can be examined. The basic principle of this technique is the interaction of light with material which provides insights into its electronic structure and band gap.

When light is incident on a material, its photons may be absorbed depending on the material's band gap energy. This absorption leads to various electronic transitions, which can be categorized into three main types:

- **Case 1: Photon energy equals band gap energy ($h\nu = E_g$)** – When the energy of the incoming photons matches the band gap energy of the semiconductor, electron-

hole pairs are generated. Electrons are excited from the valence band (Ev) to the conduction band (E_c), leaving behind holes.

- **Case 2: Photon energy exceeds the band gap ($h\nu > E_g$)** – In this scenario, electrons still transition from the valence band to the conduction band, but the excess energy (greater than the band gap) is usually released as heat rather than promoting the electron to higher conduction states.
- **Case 3: Photon energy is less than the band gap ($h\nu < E_g$)** – Electrons cannot directly transition from the valence to the conduction band. However, if the material contains impurity states or defect levels within the band gap, the electrons may still be excited via these intermediate energy states.
- The first two scenarios represent **intrinsic transitions**, where photon absorption occurs without the aid of impurity levels, requiring energy equal to or greater than the semiconductor's band gap. The third scenario involves **extrinsic transitions**, which rely on introduced defect states within the band gap to enable excitation by lower-energy photons.

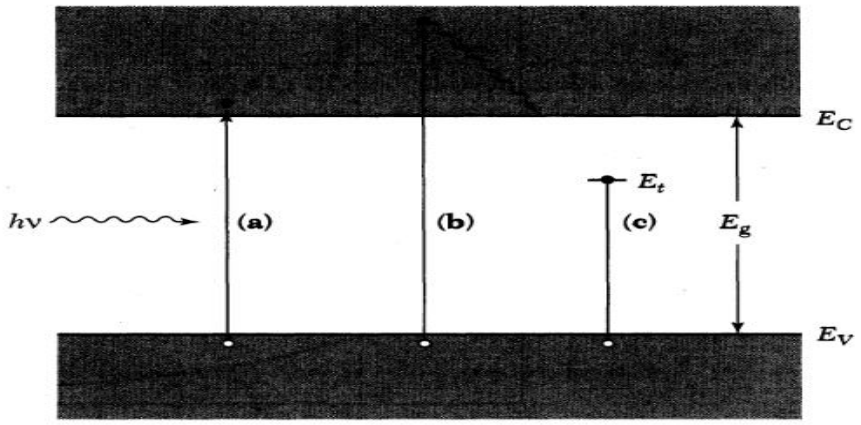

Figure 28: Different optical transitions.

A UV-Visible spectrophotometer consists of several key components. It begins with a light source, which emits a broad spectrum of light. This light then passes through a monochromator, which isolates and allows only a specific wavelength of light to pass through, making the light effectively monochromatic. The light beam is then split into two paths: one passes through the sample (typically a semiconductor), and the other through a reference material. After passing through these paths, the light reaches a photodetector,

which measures the intensity of the transmitted or absorbed light. This data is used to determine the optical properties of the sample across different wavelengths [29].

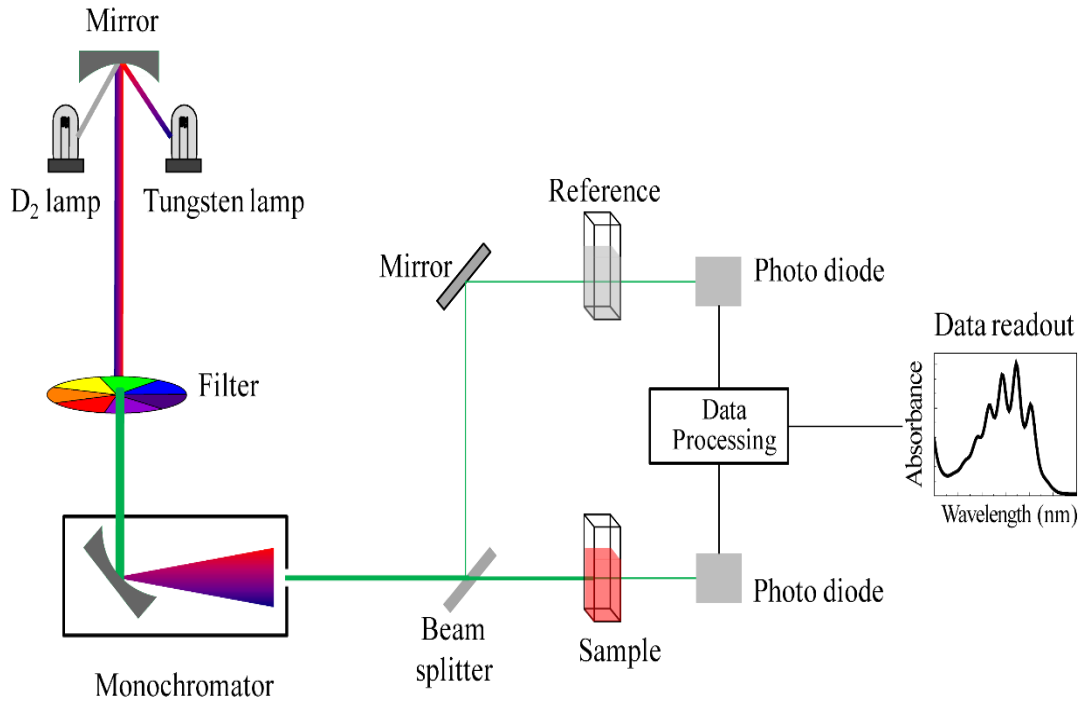

Figure 29: Schematic of UV-Vis Spectrophotometer.

By using the transmittance and reflectance data of the given sample, one can easily estimate the optical absorption coefficient and energy band gap of the sample.

The formula for optical absorption coefficient is given below-

$$\alpha = \frac{-\ln\left[\frac{-(1-R)^2 + \sqrt{(1-R)^4 + 4T^2R}^2}{2\pi R^2}\right]}{t} \qquad \ldots. (17)$$

T = transmittance

R = reflectance

t = thickness

The formula is used to calculate the energy band gap which is given below-

$$\alpha h\nu = A\left(h\nu - E_g\right)^n \quad \text{.... (18)}$$

Where n tells us about the transition whether it is direct/indirect and allowed/forbidden.

n = 2 for indirect allowed transition

n = 1/2 for direct allowed transition

n = 3/2 for direct forbidden transition

By plotting the graph between $(\alpha h\nu)^{1/2}$ and $h\nu$ and extrapolating the curve to energy axis optical band gap is estimated

E_g – semiconductor's band gap

h – Planck's constant

$h\nu$ – energy of incident photon

A – constant

ν – frequency of incident photon

4.5. OPTICAL PROFILOMETER

Optical profilometer is a non-contact thickness measurement instrument which provides the information about the roughness of surface and surface topology of the sample without disturbing the actual surface characteristics. To know the surface in three-dimensions, the fundamental approach is to direct the light. In ancient days, this analysis also provided the information about 2D, 3D surfaces, images with roughness and feature dimension data.

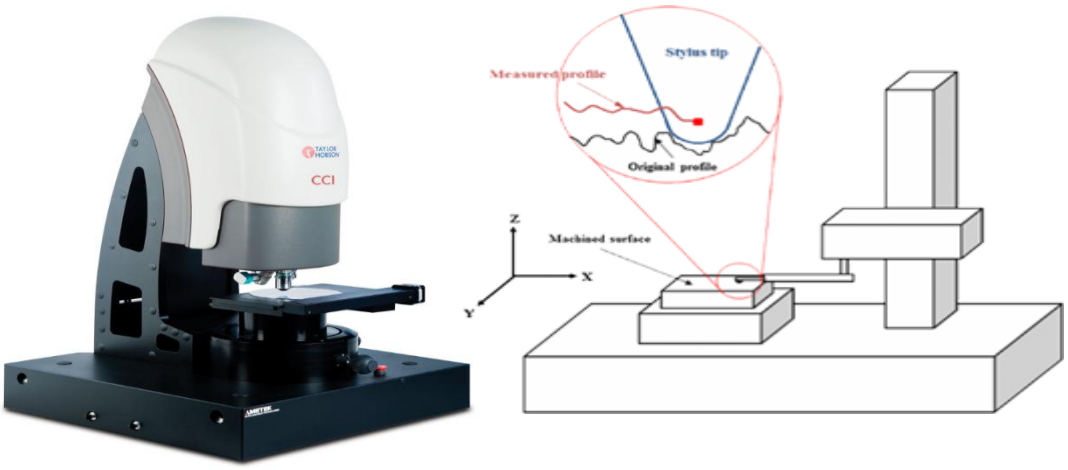

Figure 30: Optical profilometer.

Optical Profilometer gives the information about surface topology and it acts like a microscope. From the profiler lamp, the beam splitter divides the beam into two channels, one is for reference mirror and the second channel is for examining the surface. The optics is shown in the following figure –

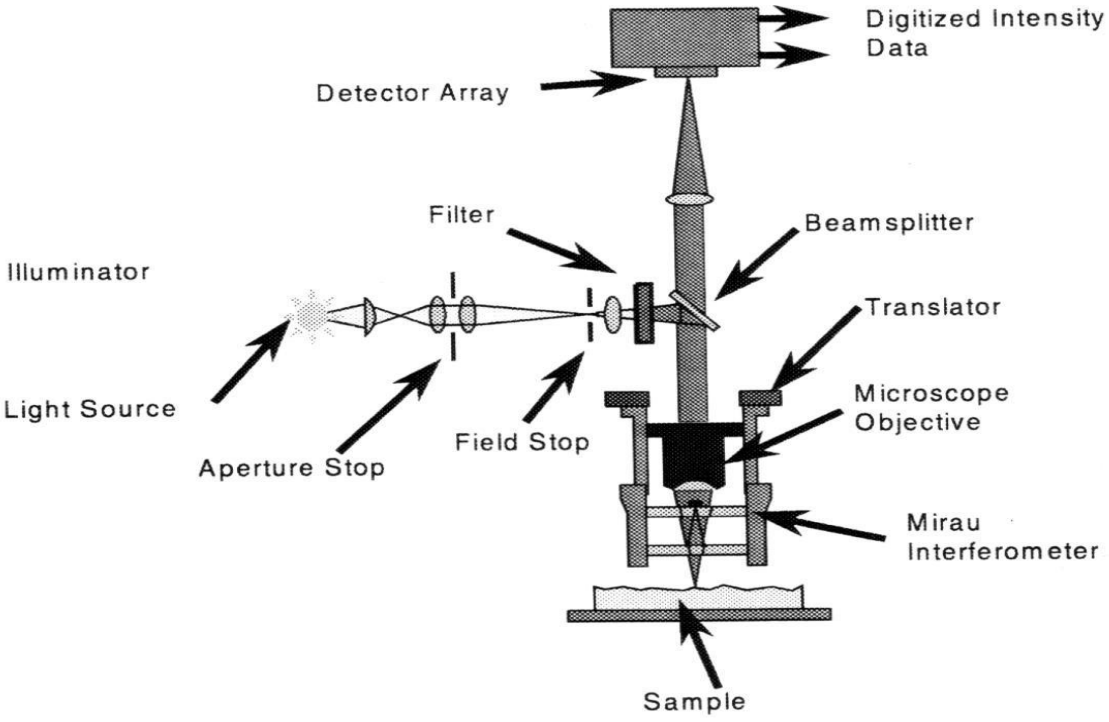

Figure 31: Schematic of Optical profilometer.

It provides a highly accurate data by allowing the data for vertical resolution up to several Angstroms. From 0.3 to 8 microns the lateral resolutions can be varied. This

technique is useful for scientific and industrial applications because it is a non-contact process so, it does not disturb the actual surface.

For examining the actual surface topology there are few terms that plays an important role in it. First one is spatial resolution that can distinguish the minute detail in longitudinal and lateral dimensions by providing a term capacity of profilometer. It can vary for the different researchers depending upon the goal and required accuracy level. A term "field of view" is defined as the entire region of material's surface that is measured by the profilometer. Second one is Image acquisition time, basically, it is essential for the data to be effective for gathering and processing basically, this variable can be affected by the kind of images, precision and frame rates [29].

4.6. HALL EFFECT MEASUREMENT SYSTEM

Hall Effect measurement provides the information about the electrical properties of the material like conductivity and the conductivity type. In this process, the electrons in *n*-types and holes in *p*-types are diverted when current flows perpendicular to the applied magnetic field. A voltage is generated when charge carriers are deflected due to the influence of a magnetic field; this is known as the Hall voltage. By analysing the polarity of this voltage, one can determine the type and effective charge of the carriers.

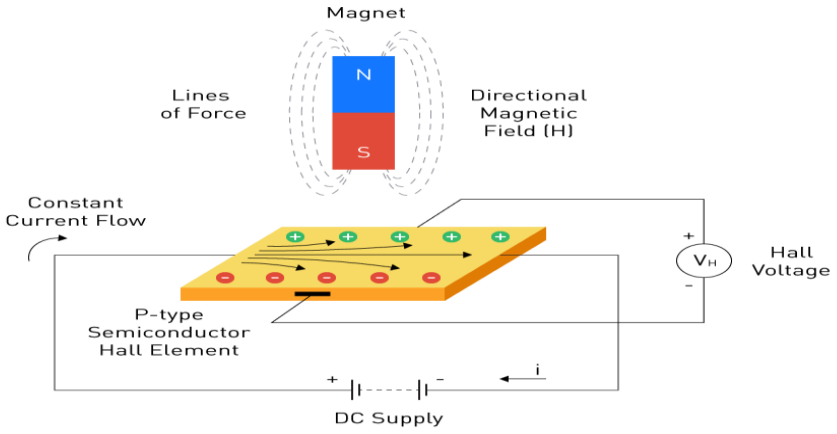

Figure 32: Hall effect schematic.

By knowing the magnetic field intensity, carrier density, and current, the magnitude of the Hall voltage can be determined. This voltage can then be used to calculate the carrier mobility.

In the figure, a thin strip of thickness *t* is shown under observation, placed in a magnetic field oriented perpendicular to the plane of the sample. The current flows from right to left, and the potential difference is measured between the top and bottom surfaces. When the magnetic field H is zero and the voltmeter probes are aligned vertically, the voltage difference is also zero.

Due to this phenomenon, charge carriers are deflected either upward or downward as a result of the Lorentz force, expressed as q (v × B). Since the charges cannot escape from the top or bottom surfaces of the strip, a vertical charge imbalance develops. This imbalance generates an electric field in the vertical direction, referred to as the Hall electric field, which counteracts the influence of the magnetic field and establishes equilibrium. The strength of this electric field can be determined by measuring the transverse potential difference using a voltmeter. [30].

The polarity of the hall voltage depends up on the type of charge carriers that are deflected, if the carriers are electrons, then a positive value of hall voltage is obtained and if they are holes, a negative value is obtained.

$$\mathbf{V_H = \frac{IB}{qnt}} \qquad \textbf{.... (19)}$$

Where B = applied magnetic field

q = charge

I = current

n = carrier density

and then by these equations, carrier density can be easily calculated,

$$\mathbf{n = \frac{IB}{qtV}} \qquad \textbf{.... (20)}$$

t – thickness

V = V_H = hall voltage

And, now by using the Van-der Pauw technique, one can get electrical information of the semiconducting sample. It is as simple as that

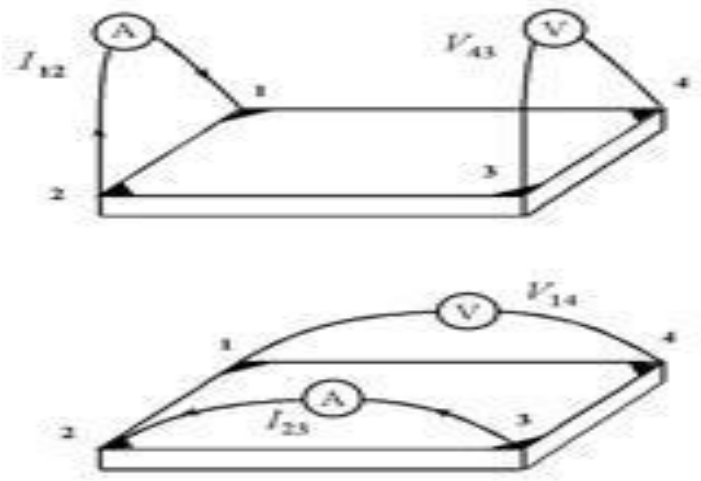

Figure 33: Van der Pauw technique.

First, current is passed between points 1 and 2, and the potential difference is measured across points 3 and 4. Then, alternatively, current is passed between points 2 and 3, and the potential difference is measured across points 1 and 4.

Figure 34: Hall Effect measurement setup for electrical measurement.

CHAPTER 5: RESULTS AND DISCUSSIONS

Results of SnSe thin films are given below that were deposited by thermal evaporation technique and characterized by different characterization techniques.

5.1. XRD ANALYSIS

By using the X-Ray diffractometer, basic structural characterization of SnSe thin films were carried out. All the thin films were deposited by thermal evaporation technique at a substrate temperature of RT, 100 ˚C, 150 ˚C and 200 ˚C. The XRD pattern of the respective samples are given below with changing the substrate temperature.

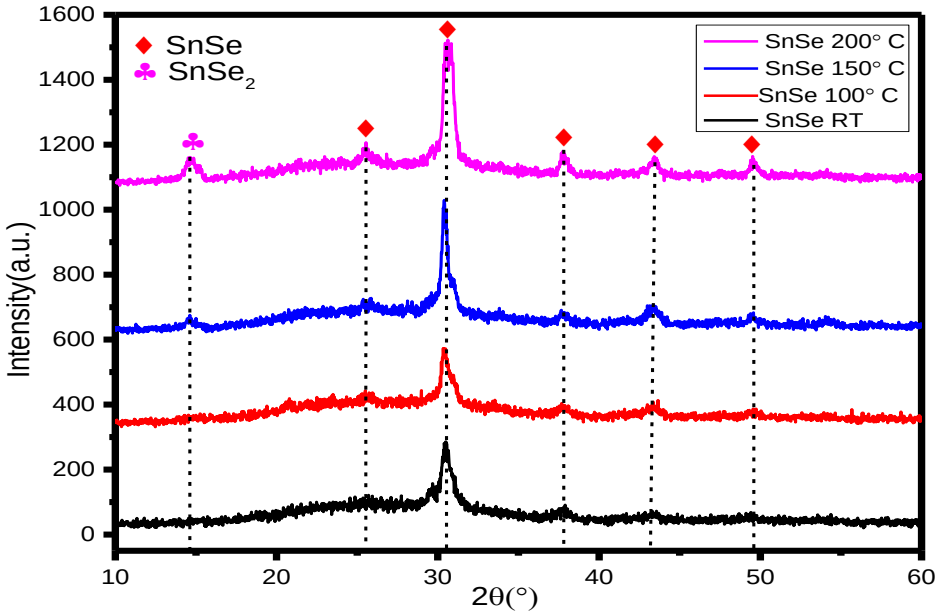

Figure 35: XRD pattern for SnSe at different substrate temperatures.

From the XRD pattern of all SnSe thin films, the highly intense peak was found to be at a 2θ values of 30.5˚, 30.48˚, 30.5˚ and 30.46˚ for all the SnSe films deposited at different substrate temperatures at RT, 100 ˚C, 150 ˚C and 200 ˚C respectively with the crystal plane (1 1 1). The SnSe thin film deposited at RT was found to be single phase that matched with the JCPDS card no. (65-3767). The SnSe thin film that was deposited at 100 ˚C also found to be single phase of SnSe and matched the data with JCPDS card no. that is (89-0232) and the films that were deposited at high temperatures of 150 ˚C and 200 ˚C was found to have two phases. With the primary phase of SnSe along with some traces of $SnSe_2$ phase

of (0 0 1) plane at a 2θ value of 14.66˚ which matched with the data of JCPDS card no. (89-3197) and may be due to the decomposition of selenium at higher temperature.

From the XRD data, it was concluded that all the thin films were polycrystalline in nature with low crystallinity which might be due to the insufficient annealing time.

Then, the crystallite size for the films deposited at 150 ˚C and 200 ˚C were calculated by using the Debye Scherrer's formula given in equation (16)-

Table 5: Average crystallite size of SnSe films deposited at different substrate temperatures.

Substrate temp. (˚C)	Average crystallite size (nm)
150	15.33
200	10.53

We were not able to calculate the data for average crystallite size for deposited films at RT and 100 ˚C due to very low peak intensities in XRD pattern.

Then, the lattice parameters a, b, and c for SnSe thin films deposited at different substrate temperatures were calculated and are shown in the given table

Table 6: Lattice parameters for SnSe thin films deposited at different substrate temperatures.

Substrate temp. (˚C)	Lattice parameters (Å)
RT	a = 11.55, b = 4.19, c = 4.42
100	a = 11.55, b = 4.18, c = 4.40
150	a = 11.55, b = 4.18, c = 4.68
200	a = 11.55, b = 4.14, c = 4.41

By considering the lattice parameters of different SnSe thin films, it was found that all the SnSe thin films deposited are orthorhombic in structure [23].

It was concluded by the XRD data that with increase in the substrate temperature for deposition of SnSe thin films, the crystallinity was slightly increased due to the sufficient energy for atoms to arrange periodically.

5.2. RAMAN ANALYSIS

By using the Raman spectroscopy of the thin films of SnSe deposited at different substrate temperatures, it was found that the deposited thin films were not in the single phase. There were some traces of secondary phase of $SnSe_2$ along with primary SnSe phase. Phonons vibrational modes were investigated for nanostructured SnSe thin films and it was found that there were two modes, one for SnSe and another is for $SnSe_2$. For SnSe there was a peak at 154 cm^{-1} associated with A_{3g} Raman active mode and for $SnSe_2$ at 182 cm^{-1} associated with A_{1g} Raman active mode [22].

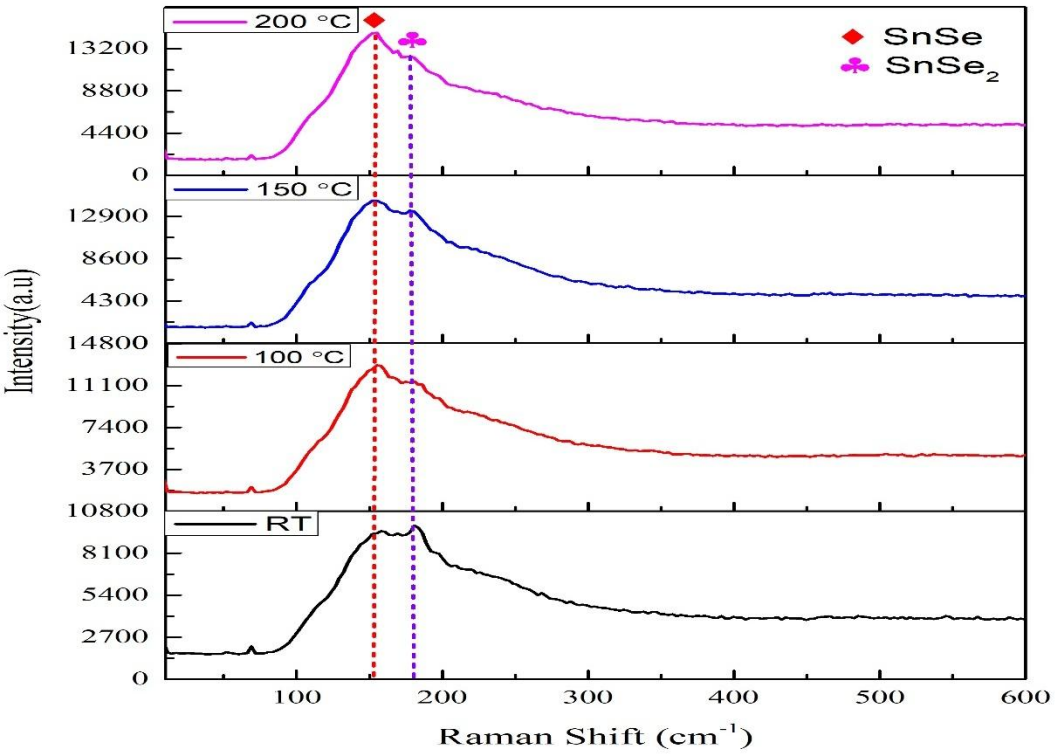

Figure 36: Raman spectra for SnSe films deposited at different substrate temperatures.

5.3. MORPHOLOGICAL ANALYSIS

The surface morphological analysis was carried out by FE-SEM (Field Emission Scanning Electron Microscope) of the prepared SnSe thin films deposited at different substrate temperatures. The images by the FE-SEM of the deposited SnSe thin films are shown below –

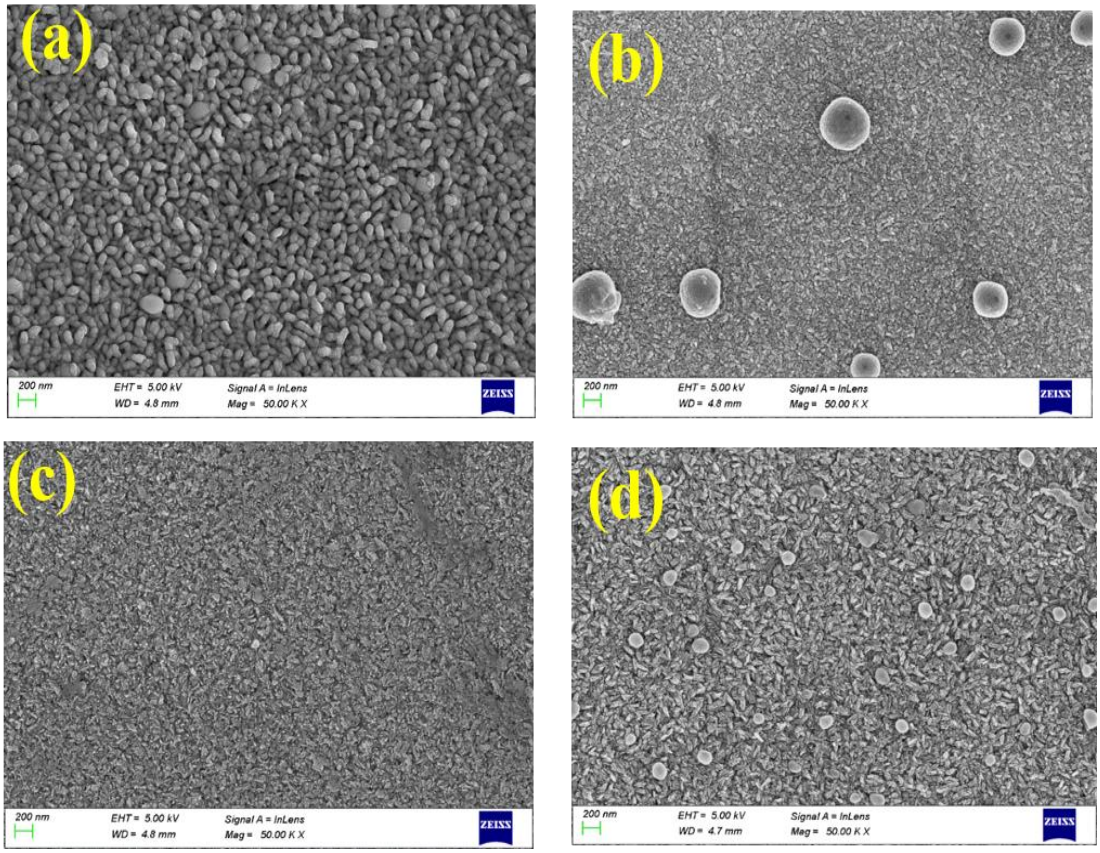

Figure 37: FE-SEM images of SnSe deposited at different substrate temperatures, (a) RT, (b) 100 ˚C, (c) 150 ˚C and (d) 200 ˚C.

From the FE-SEM images, it was observed that SnSe film deposited at RT showed larger grains compared to films deposited at other temperatures. Films deposited at 100 ˚C and 150 ˚C showed smaller grains with compact surface morphology which may be due to sufficient substrate temperature for the arrangements of atoms. While the film deposited at 200 ˚C showed slightly bigger grains with few agglomerates present on the surface which may be due to the $SnSe_2$ phase present at higher temperatures due to the decomposition of Se which might react with SnSe and resulted in formation of $SnSe_2$ agglomerates.

5.4. COMPOSITIONAL ANALYSIS

The compositional analysis of the SnSe thin films deposited at different substrate temperatures was carried out by SEM equipped with EDX, the following table shows the results of composition in prepared SnSe thin films.

Table 7: Elemental atomic percentage in deposited SnSe thin films.

Element	RT	100 ˚C	150 ˚C	200 ˚C
Sn (%) L	47.72	47.05	46.68	46.67
Se (%) L	52.28	52.95	53.32	53.33

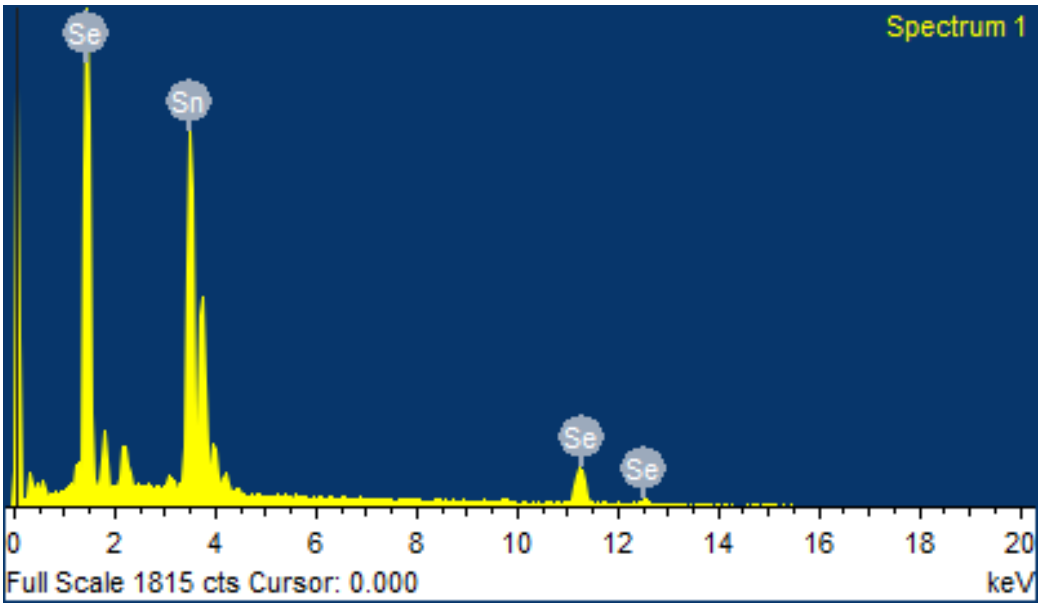

Figure 38: EDS spectra for SnSe thin film deposited at RT.

From the data, it was concluded that there was slight difference in composition with deposition temperatures. As the substrate temperature increased the atomic percentage of Se observed to be increased slightly. This may be due to the decomposition of SnSe during deposition which reacted with SnSe and leading to the formation of secondary phase of $SnSe_2$. This was confirmed by the XRD and Raman analysis. Figure 38 shows the EDS spectra of SnSe film deposited at RT indicating the Se rich composition.

5.5. OPTICAL ANALYSIS

By using JASCO V770 spectrophotometer, the UV-Visible NIR spectra of the deposited SnSe thin films was obtained. The spectra were recorded in the range from 500 nm to 2500 nm. The transmittance and reflectance of the prepared SnSe thin films deposited at different substrate temperatures are shown below in the figure 39.

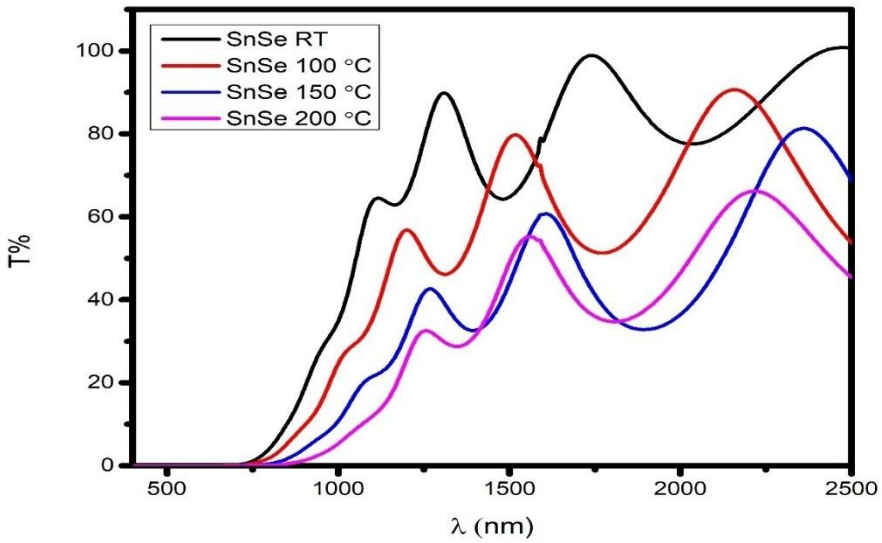

Figure 39: Transmittance spectra for deposited SnSe thin films deposited at different substrate temperatures.

The transmittance percentage decreased as the substrate temperature of SnSe thin films varied from RT to 200 ˚C which might be due to reduced grain sizes.

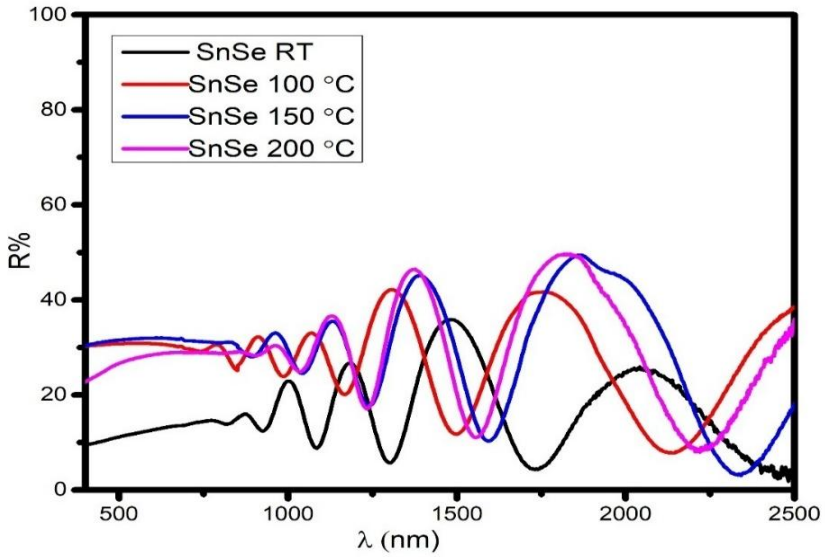

Figure 40: Reflectance spectra for deposited SnSe thin films deposited at different substrate temperatures.

From the reflectance spectra, it was observed that at higher temperatures, the reflectance found to be nearly same, but as the substrate temperature decreased to room temperature its reflectance becomes low.

Using R%, T% and thickness of deposited SnSe thin films at different substrate temperatures, the absorption coefficient was calculated by using the given formula

$$\alpha = \frac{-ln\left[\frac{-(1-R)^2 + \sqrt{(1-R)^4 + 4T^2R}^2}{2\pi R^2}\right]}{t}$$

From the data of absorption coefficient and energy of incident photon, optical direct band gaps were calculated and are shown in the given figure 41.

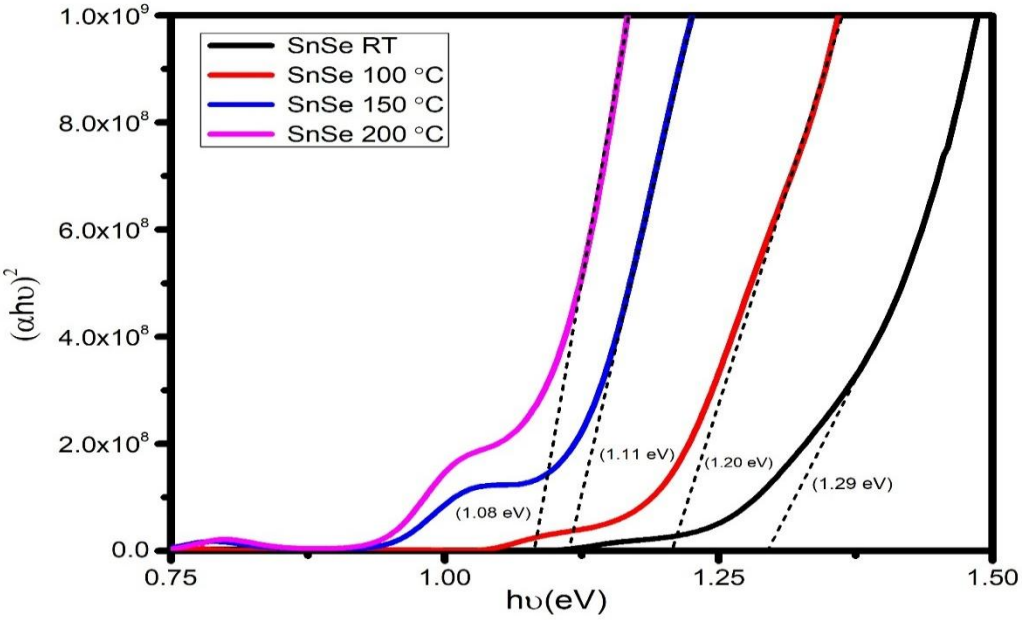

Figure 41: Optical direct band gaps for different SnSe thin films at different substrate temperatures.

The optical band gaps of SnSe thin films deposited at different temperature observed to decrease with increase substrate temperature to RT to200 ˚C. The band gaps for SnSe films deposited at a substrate temperature of RT, 100 ˚C, 150 ˚C and 200 ˚C was found to be 1.29, 1.2, 1.11 and 1.08 eV respectively. The optical band gap of the films found to decrease with increase in substrate temperature and it might be due to the better crystallinity of SnSe thin films as evident from XRD pattern.

5.6. THICKNESS ANALYSIS

By using a non-contact process of optical profilometer the thickness of SnSe thin films deposited at different temperatures were calculated.

Table 8: Thickness of deposited SnSe thin films at different substrate temperature.

Deposited film	Substrate temperature (˚C)	Thickness (nm)
SnSe	RT	646
SnSe	100	631
SnSe	150	637
SnSe	200	634

The above table shows the thicknesses of the SnSe thin films deposited at different substrate temperatures. It was observed that for all the thin films the thickness was observed to be nearly equal and close to the value (600 nm) which was monitored during deposition by QTM.

5.7. ELECTRICAL PROPERTIES

By using the Hall effect measurement set up was used to measure the electrical properties of all the deposited SnSe thin films which were deposited at different substrate temperatures. During measurements 1T of magnetic field and 0.2 μA current was applied to the sample. In the table 9 shown below, electrical properties like resistivity, mobility, carrier density and conductivity of the films are given.

Table 9: Electrical properties of deposited SnSe thin films at different substrate temperatures.

Substrate temperature (˚C)	Carrier concentration (cm^{-3})	Mobility ($cm^2/V\text{-}s$)	Resistivity (Ω-cm)	Conductivity type
RT	1.182×10^{16}	2.754×10^{-1}	1.951×10^{3}	*p*
100	6.21×10^{16}	4.73×10^{0}	2.125×10^{1}	*p*
150	2.64×10^{18}	1.04×10^{0}	2.274×10^{0}	*p*
200	4.246×10^{18}	1.547×10^{1}	9.501×10^{-2}	*p*

From the observation table, we found that all SnSe thin films prepared at different substrate temperatures exhibit *p*-type conductivity. As the substrate temperature increased from room temperature (RT) to 200 °C, the resistivity decreased from the order of 10^3 to 10^{-2} Ω-cm, and the mobility increased from 0.27 to 15 cm^2/Vs. The carrier concentration of the SnSe samples also increased from the order of 10^{16} to 10^{18} cm^{-3} with increasing substrate temperature. These variations might be attributed to the improved crystallinity of the SnSe films at higher substrate temperatures, as observed from the XRD analysis. Additionally, the changes could be due to the increased compactness of SnSe particles at higher substrate temperatures, as indicated by the SEM images.

5.8. THERMOELECTRIC MEASUREMENTS

As already mentioned, that thermoelectric effect is the conversion into electricity or voltage by introducing some temperature gradient at two different ends of the material [9]. Now, the thermoelectric observations for different SnSe thin films deposited at different substrate temperature are shown in table-

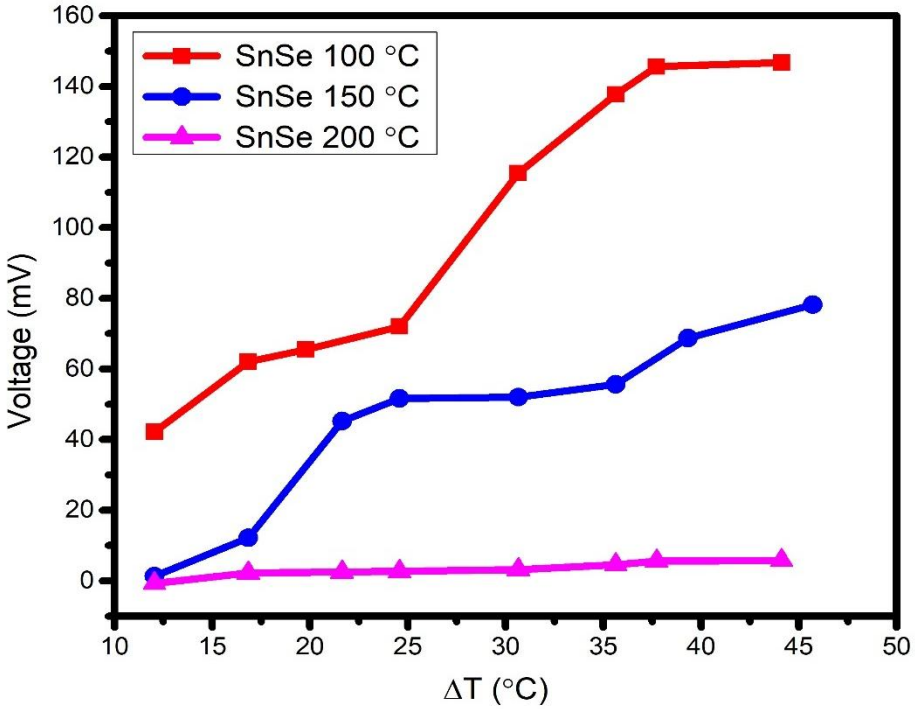

Figure 42: Plot of thermos emf Vs ΔT of SnSe thin films deposited at different temperatures.

Table 10: Different Seebeck coefficients for different SnSe thin films.

SnSe deposition temperature (˚C)	Seebeck coefficient (mV/ ˚C)
100	3.7
150	2.125
200	0.18

From the figure 42 and observation table, it was clearly observed that SnSe deposited at 100 ˚C was found to be a good thermoelectric material due to its high value of Seebeck coefficient as compare to SnSe thin films deposited at 150 ˚C and 200 ˚C. This might be due to the increased crystallinity and carrier concentration of SnSe film as evident from XRD and electrical measurements respectively.

CHAPTER 6: APPLICATION

6.1. GAS SENSOR

A Gas sensor is a device which detects the gas in a particular area by giving some type of electrical signal [2]. Here, we specifically chose our SnSe thin film as a sensing material which was deposited at a substrate temperature 200 ˚C. In our case, the change in the electrical resistance of the sensing material which is SnSe thin film from the resistance value [4] measured at respective temperatures using the Keitley 2612 B set up.

As per the literature review, it was observed that SnSe is highly sensitive to NO_2 gas which is an oxidizing gas which reduces the natural resistance value of SnSe thin film which is a sensing material and provides a response from 174% to 700% depending upon the morphology. And by the literature survey, we observed that SnSe nanostructured thin film is highly selective to NO_2 type gas and provides a good response at room temperature with a very high response and recovery time [19].

As per the literature survey SnSe thin films were tested as a gas sensing materials for different types of gases like NO_2, NO, NH_3, H_2, SO_2, H_2S, CO_2, CH_4 etc. [19][20] and it was observed that they were highly selective for only NO_2 type gases. SnSe has also shown the ability to sense CH_4 gas with a 47% of response at 200 ˚C [19], that is why we chose the SnSe thin film which was deposited at 200 ˚C as a sensing material to detect LPG. We specifically chose LPG gas which is made up of hydrocarbons and has a primarily content of Propane (C_3H_8) and Butane (C_4H_{10}). By considering the possibility that SnSe will show some response to LPG in the low concentration.

To cross-check whether SnSe thin film is selective for only NO_2 or for any other hydrocarbon type of gases. LPG is also a reducing, combustible and harmful gas, so it is important to detect these types of gases in the environment or in residential areas.

Before going to the testing of SnSe thin film as a sensing material for LPG detection, first we have to understand some of the terminologies which is associated with a gas sensor.

Terminologies

- ✓ **Sensitivity or Response percentage** – So, basically it tells us about that how effectively our device detects that gas even in its low concentration [3].

$$\textbf{Sensitivity} = | R_a - R_g | / R_a$$

R_a – Natural resistance value of sensing material without gas

R_g – Resistance of sensing material after inserting the gas when it was saturated.

- ✓ **Response time –** It indicates how fast our device works and will provide an electrical signal, even in the low concentration of gas [4].
  It is the time taken by the device to go to the 90% of the saturation value of the natural resistance after purging the gas [31].

  In the given figure, let us understand the response time.

  So, it is the time just after the gas insert, when the resistance has been saturated, resistance value may get reduced or increased depending upon the type of gas which was inserted whether it is oxidizing or reducing.

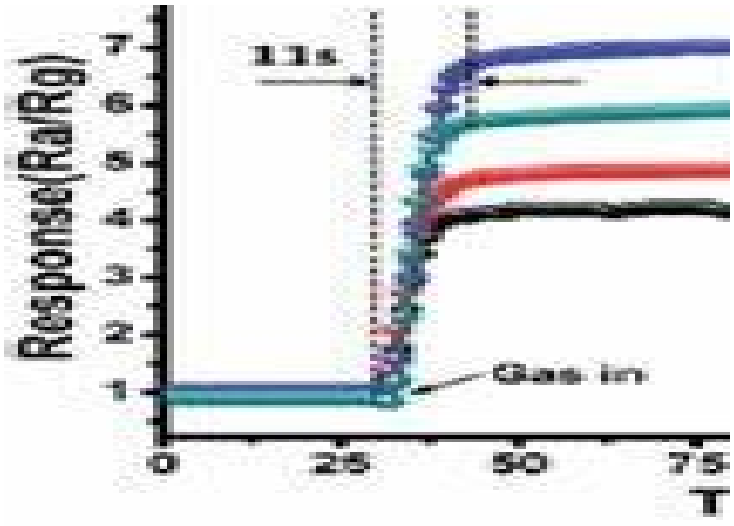

Figure 43: Diagram of response time after gas.

- ✓ **Recovery time –** It tells us about that how much time will the device take to come to its 90% of initial value of resistance after the gas was ejected [31].

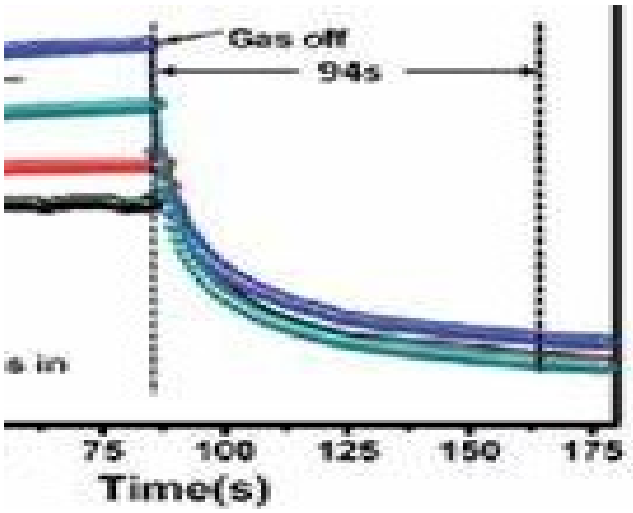

Figure 44: Diagram of recovery time after the gas was ejected.

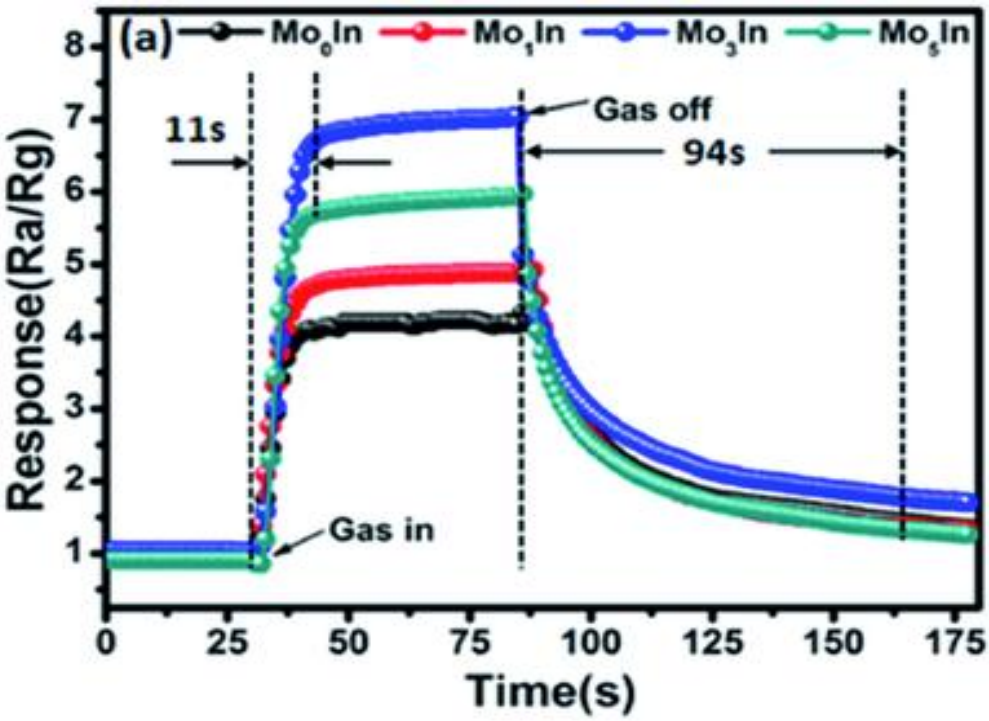

Figure 45: Response and recovery time of a gas sensor.

How to measure ppm (parts per million)

ppm – parts per million

So, basically it is a measurement tool, if we divide any volume in one million parts then its one part is said to be 1 ppm.

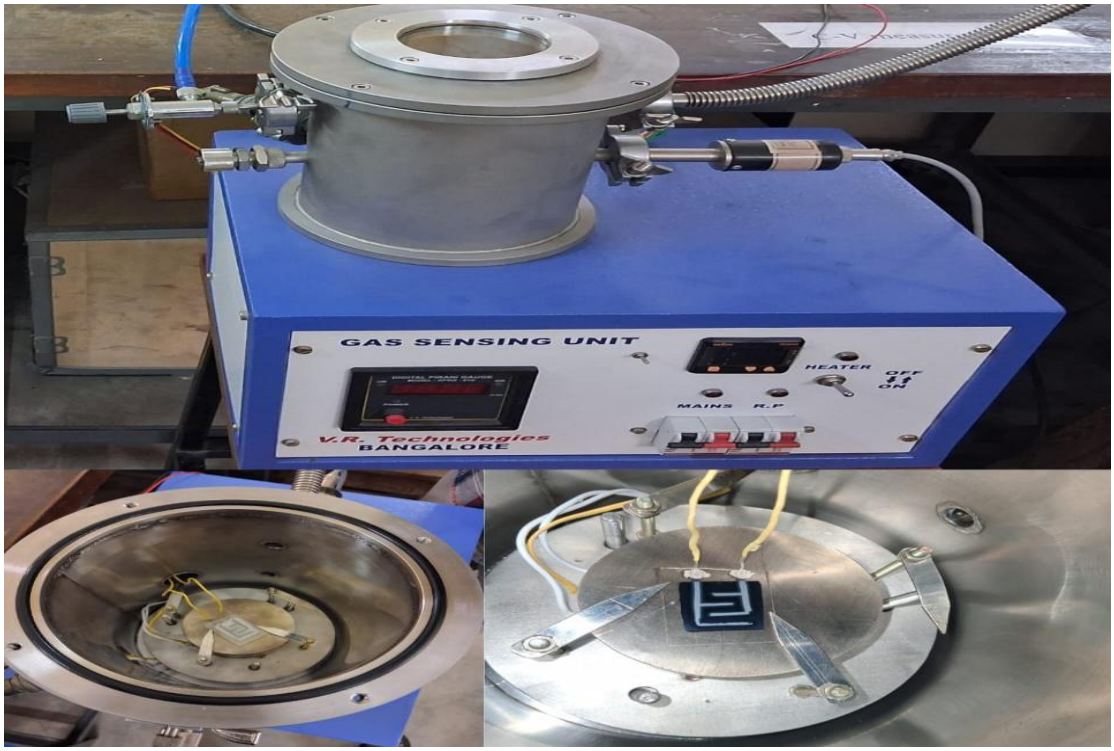

Figure 46: Gas sensing material inside the vacuum chamber.

Now, the volume of the chamber = 3150 cm^3

We know that, 1 m^3 = 1000 litres ---------- (1)

And 1 m^3 = 10^6 cm^3 ---------- (2)

From equation (1) and (2), we get

10^6 cm^3 = 1000 litres and 1000 cm^3 = 1 litre

This means that, 1 cm^3 = 1/1000 litre

and 3150 cm^3 = (1/1000) × 3150 = 3.15 litres

Therefore, Volume of the chamber = 3.15 litres

Now, dissociate the volume of the chamber into 1 million parts which means that 3.15 litres = 10^6 ppm

3150 ml = 10^6 ppm

1 ml = 10^6/3150 = 317.46 ppm and 0.1 ml = 31.7 ppm

So, if we have a pipette of 10 ml, then its least count is 0.1 ml. It contains a least gas of about 31.7 ppm.

Then, by doing the rough estimation,

50 ppm = (0.1/31.7) × 50 = 0.157 ml, Similarly

100 ppm = 0.31 ml roughly around 0.3 ml

150 ppm = 0.47 ml roughly around 0.45 ml

200 ppm = 0.628 ml roughly around 0.65 ml

250 ppm = 0.785 ml roughly around 0.9 ml

300 ppm = 0.942 ml roughly around 1 ml

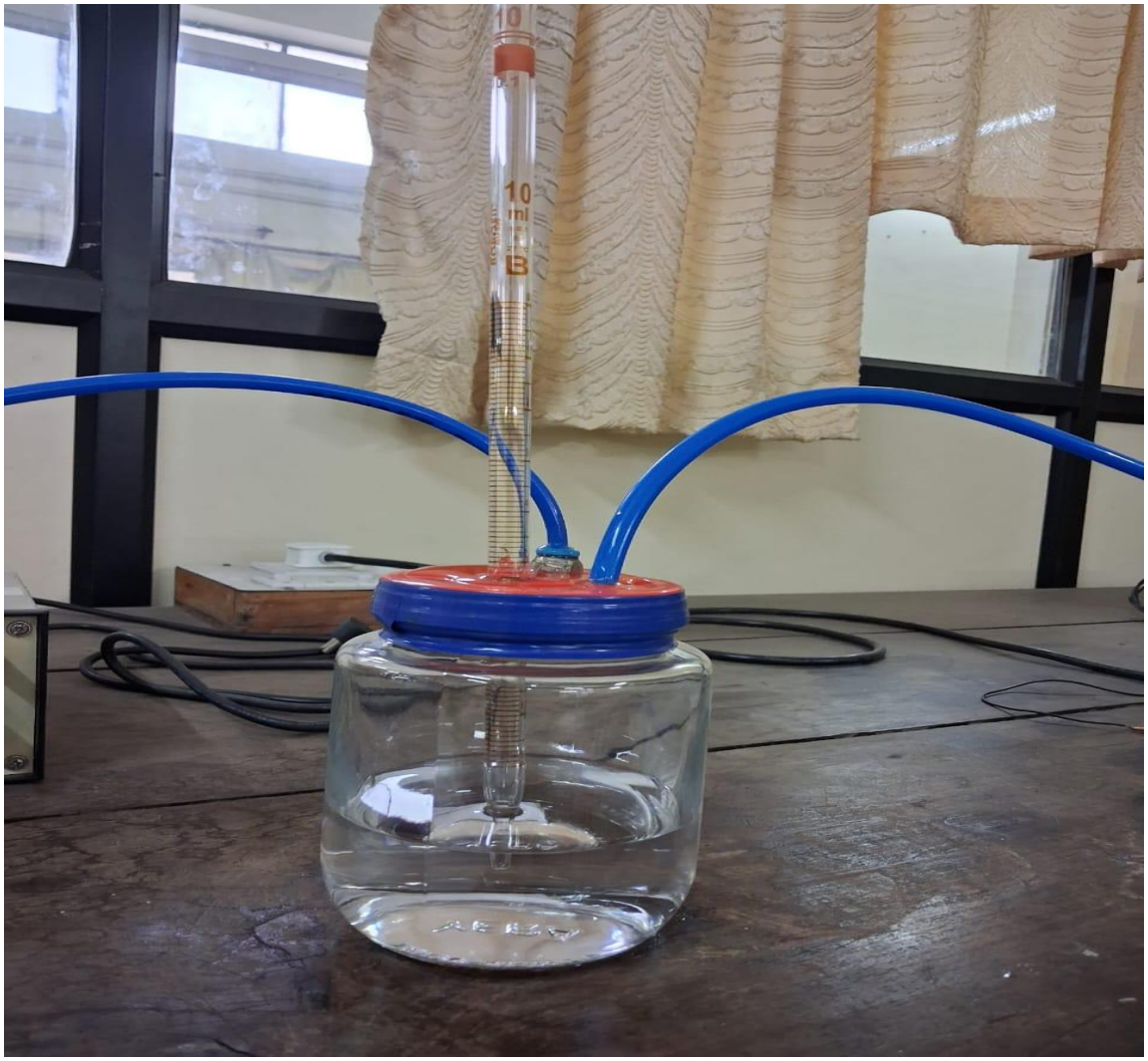

Figure 47: Measuring set up for gas using a pipette and a glass jar.

6.1.1. Temperature variation during measurements

As per by the testing of SnSe thin film deposited at 200 ˚C as a sensing material for LPG detection, it did not show the good results at room temperature. There were some fluctuations in the resistance value after inserting the gas of about 50-250 ppm. Because of this, the resistance value did not saturate at any value. Then, it was decided to increase the temperature at a step of 30 ˚C. As per literature review SnSe thin film detects CH_4 gas at 200 ˚C. Hence, we have decided to do the observations by providing the temperature at 60 ˚C and 90 ˚C.

Figure 48: Gas sensing setup with LPG cylinder, jar, gas sensing unit with chamber connected with rotary pump and laptop.

6.1.1.1. At a temperature of 60 ˚C

The temperature of 60 ˚C was provided to the sensing material placed in vacuum chamber and LPG gas was inserted from 50 ppm to 150 ppm.

(i) At 50 ppm – The response at 60 ˚C is shown in the figure 49.

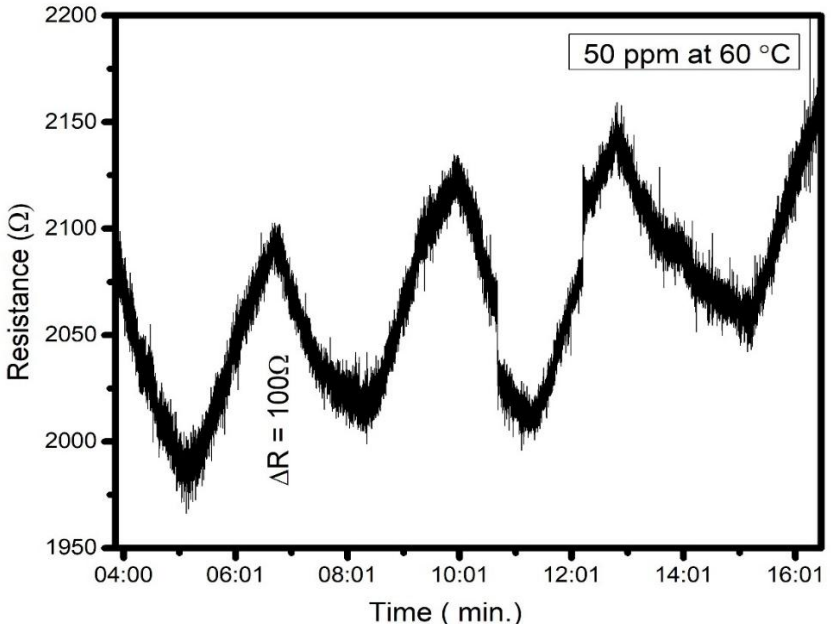

Figure 49: LPG response for SnSe sensing material at 50 ppm.

The natural resistance value observed to vary from 2100 Ω to 2150 Ω.

Response time = 58 seconds

Recovery time = 65 seconds

Sensitivity, R% = ((2100 – 2000)/2100) × 100 = 4.76%

(ii) At 100 ppm – The response at 60 ˚C is shown in the figure 50.

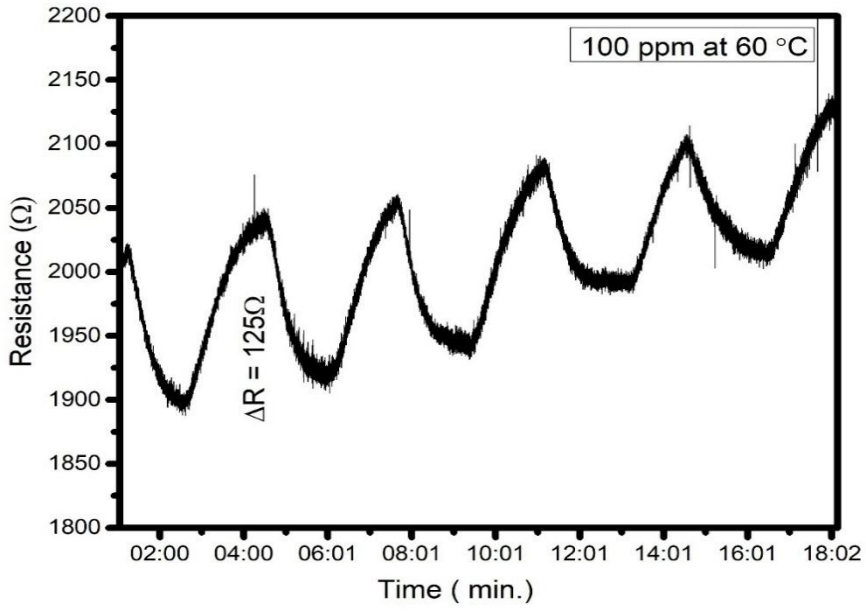

Figure 50: LPG response for SnSe sensing material at 100 ppm.

The natural resistance was observed to vary from 2025 Ω to 2100 Ω.

Response time = 49 seconds

Recovery time = 72 seconds

Sensitivity, R% = 6.172%

(iii) At 150 ppm – The response for 150 ppm 60 ˚C is shown in the figure 51.

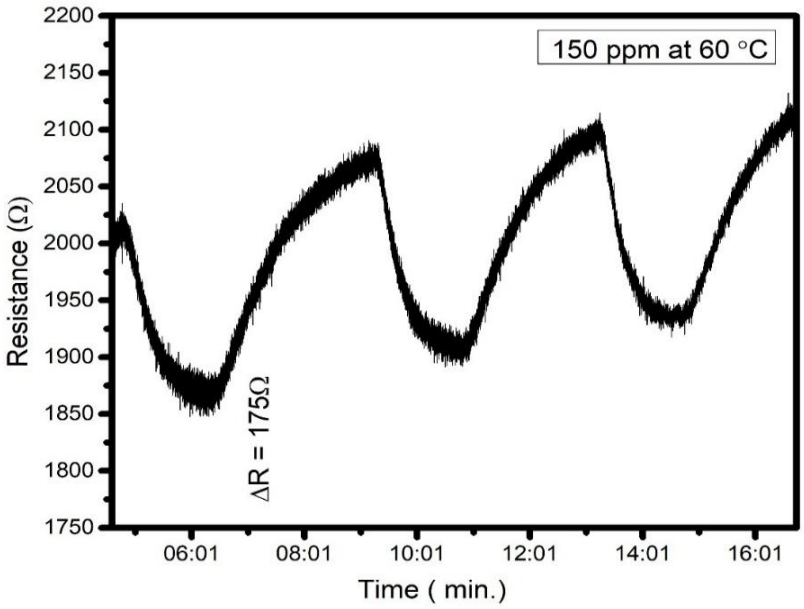

Figure 51: LPG response for SnSe sensing material at 150 ppm.

Natural resistance value was observed to change from 2025 Ω to 2100 Ω.

Response time = 43 seconds

Recovery time = 107 seconds

Sensitivity, R% = 8.43%

(iv) For < 50 ppm – The response of <50 ppm of LPG at 60 ˚C is shown in figure 52.

Due to the limitation of the set-up, exact measurements of the gas less than 0.1 ml are not possible. Hence, a rough estimation was made to insert the gas less than 50 ppm.

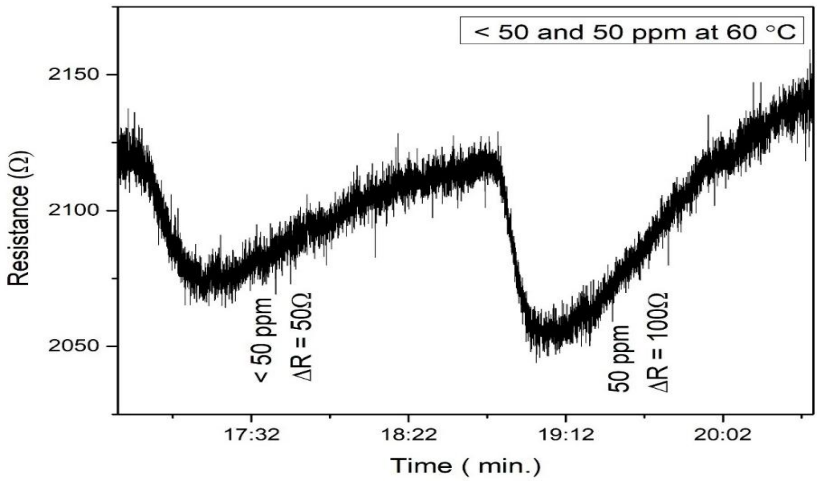

Figure 52: LPG response for SnSe sensing material for less than 50 ppm.

Response time = 27 seconds

Recovery time = 50 – 60 seconds

Sensitivity, R% = 2.35%

6.1.1.2. At a temperature of 90 ˚C

Temperature of the device was increased from 60 ˚C to 90 ˚C in vacuum chamber. The figure 53 shows the device response at different concentrations of LPG gas from 200 to 300 ppm –

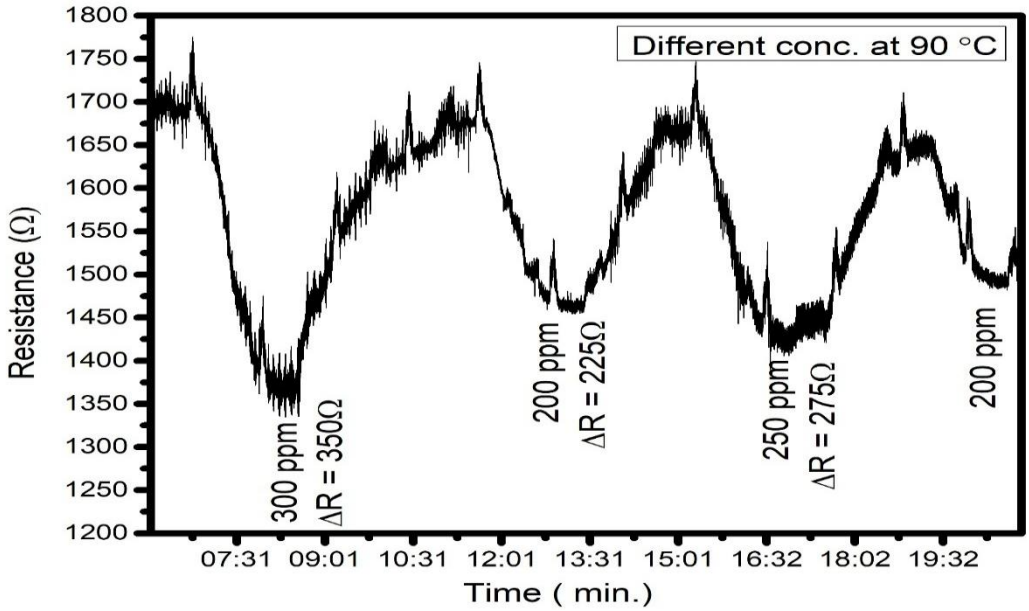

Figure 53: LPG response for SnSe as a sensing material for different concentrations at 200 ppm, 250 ppm and 300 ppm.

✓ **For 200 ppm –**

Response time = 51 seconds

Recovery time = 85 seconds

Sensitivity, R% = 13.23%

✓ **For 250 ppm –**

Response time = 48 seconds

Recovery time = 91 seconds

Sensitivity, R% = 14.7%

✓ **For 300 ppm –**

Response time = 46 seconds

Recovery time = 98 seconds

Sensitivity, R% = 19.12%

6.1.2. Discussion on sensing results

- **At 60 ˚C**

Table 11: Different responses for LPG by taking SnSe as a sensing material at 60 ˚C at different concentrations.

Concentration of LPG gas (ppm)	Response time (sec)	Recovery Time (sec)	Sensitivity, R%
< 50	27	50-60	2.35
50	58	65	4.76
100	49	72	6.17
150	43	107	8.43

- **At 90 ˚C**

Table 12: Different responses for different concentration of LPG gas by using SnSe as a sensing material at 90 ˚C.

Concentration of LPG gas (ppm)	Response time (sec)	Recovery time (sec)	Sensitivity, R%
200	51	85	13.23
250	48	91	14.7
300	46	98	19.12

From the detection of LPG gas in various concentrations by SnSe thin film with Ag finger type electrodes, it was observed that at 60 ˚C, as the concentration of the gas was increased the gas sensitivity was increased from 2.35 to 8.43% and its response time was found to vary from 27 to 58 seconds indicates that its response time is high. Recovery time was observed to increase from 50 to 107 seconds as the concentration of LPG gas increased.

For 90 ˚C, it was observed that responsivity was found to be high. As we increase the concentration of LPG gas from 200 to 300 ppm sensitivity changed from 13.23 to 19.12% and its response and recovery time was found to be good. Response time got decreased from 51 to 46 seconds as we increase concentration of gas and recovery time got increased from 85 to 98 seconds as we increase the concentration of gas from 200 to 300 ppm.

CHAPTER 7: SUMMARY AND CONCLUSION

7.1. SUMMARY

SnSe thin films were deposited onto glass substrates by using the thermal evaporation method at different substrate temperatures (RT, 100 ˚C, 150 ˚C and 200 ˚C). The characterizations of the SnSe thin films were carried out by suitable characterization techniques like XRD, Raman, FESEM-EDX, UV-Vis-NIR, Optical profilometer, Hall effect and thermoelectric measurements.

From XRD data, it was found that there was a single phase of SnSe present at RT and 100 ˚C. But with increasing the deposition temperature, it was observed that a binary phase of $SnSe_2$ was formed along with SnSe phase. The crystallite size was found to be 15.33 and 10.53 nm for 150 ˚C and 200 ˚C respectively the grown SnSe films found to have orthorhombic crystal structure with $a \neq b \neq c$.

Prepared SnSe thin films were also analysed using the Raman spectroscopy. It also confirmed the presence of primary SnSe phase along with secondary $SnSe_2$ phase.

By using FESEM-EDX, it was found that the surface morphology was nanostructured but with small agglomerates and the composition was found to be nearly stoichiometric with a very less variations for different SnSe thin films.

By using the UV-Visible spectroscopy, the transmittance and reflectance data was obtained for different SnSe thin films and it was found that as the deposition temperature increased the optical direct band gap decreased from 1.29 to 1.08 eV and it was found that transmittance would be higher at lower temperatures.

Thickness measurement was done by using optical profilometer and it was found that the thickness was nearly the same as measured by the DTM.

Hall effect measurement setup based on four probes technique, provided the electrical properties like carrier concentration, resistivity, conductivity, mobility and conductivity type. It was found that all the deposited SnSe thin films at different substrate temperatures having a *p*-type conductivity.

7.2. CONCLUSION

SnSe thin film was deposited at 200 ˚C with finger type Ag electrodes by using the Thermal evaporation technique. It was observed that it showed a good response to LPG gas at 60 ˚C and 90 ˚C operating temperature with a high response time and sensitivity, but it was not as good as for NO_2. The sensitivity was found to vary from 2% to 20% which is quiet low as compared to NO_2 [19]. From these results, it was concluded that SnSe thin film as a gas sensing material is not selective for LPG type gases if it has a nanostructured morphology. It was cross-checked that SnSe nanostructured thin films are highly selective and responsive for NO_2 type gases. In this study it was found that the Seebeck coefficient for SnSe thin film at 100 ˚C was found to be highest among all the deposited thin films and was found to be 3.7 mV/ ˚C which may be due to the low crystallinity and low thermal conductivity of the film.

7.3. FUTURE SCOPE

From the present work, SnSe thin films was found to be polycrystalline with some traces of $SnSe_2$ phase. So, in future the focus will be on synthesising a single phase SnSe thin films by controlling the parameters like deposition rate. This could potentially lead to significantly improved performance in sensing LPG and other hydrocarbon gases, as well as enhanced thermoelectric properties. Also, there will be a scope to test the hydrocarbon type gases by using SnSe films as a sensing material and to cross-check the selectivity and sensitivity of the material.

REFERENCES

[01] U.S. Environmental Protection Agency “Analytical methods for air quality standards.” Apti course no. 464 [version no. 4.0]

[02] Z. Yunusa, M. N. Hamidon, S. Profile, Z. Awang, A. Kaiser, and Z. Awang, “Gas Sensors: A Review,” 2014. [Online]. Available: http://www.sensorsportal.com

[03] “Compendium of chemical hazards: Liquefied Petroleum gas (LPG).”

[04] G. Korotcenkov, “Integrated Analytical Systems Series Editor: Radislav A. Potyrailo Handbook of Gas Sensor Materials.” [Online]. Available: http://www.springer.com/series/7427

[05] S. Li, W. Tang, S. Chen, Y. Si, R. Liu, and X. Guo, “Flexible Organic Polymer Gas Sensor and System Integration for Smart Packaging,” Advanced Sensor Research, vol. 2, no. 11, Nov. 2023, doi: 10.1002/adsr.202300030.

[06] G. Martinelli and M. C. Carotta, “Thick-film gas sensors,” 1995.

[07] R. A. Zargar, P. A. Ahmad, M. A. S. Gogre, and M. M. Hassan, “Screen printing coating of $(ZnO)_{0.8}(CdO)_{0.2}$ material for optoelectronic applications,” Opt Quantum Electron, vol. 52, no. 9, Sep. 2020, doi: 10.1007/s11082-020-02511-5.

[08] F. T. Z. Toma, Md. S. Rahman, K. Md. A. Hussain, and S. Ahmed, “Thin Film Deposition Techniques: A Comprehensive Review,” Journal of Modern Nanotechnology, vol. 4, p. 6, Nov. 2024, doi: 10.53964/jmn.2024006.

[09] X. Zhang and L. D. Zhao, “Thermoelectric materials: Energy conversion between heat and electricity,” Jun. 01, 2015, Chinese Ceramic Society. doi: 10.1016/j.jmat.2015.01.001.

[10] K. S. Ong, L. Jiang, and K. C. Lai, “Thermoelectric Energy Conversion,” in Comprehensive Energy Systems: Volumes 1-5, vol. 4, Elsevier, 2018, pp. V4-794-V4-815. doi: 10.1016/B978-0-12-809597-3.00433-8.

[11] “Seebeck and Peltier Effects.” "Thermoelectric Effect," Wikipedia, The Free Encyclopedia http://en.wikipedia.org/w/index.php?title=Thermoelectric_effect&oldid=53657667.

[12] P. Levinský and P. L. Synthesis, “Synthesis, Characterization and Optimization of New Thermoelectric Materials,” 2018. [Online]. Available: http://www.culture.gouv.fr/culture/infos-pratiques/droits/protection.htm

[13] “The Fundamentals of Thermoelectrics A bachelor’s laboratory practical.”

[14] A. Sharma and G. Gupta, “Recent development and prospects for metal Selenide-based gas sensors,” Apr. 01, 2023, Elsevier Ltd. doi: 10.1016/j.mseb.2023.116333.

[15] E. Llobet, “Transition metal dichalcogenide based toxic gas sensing,” Feb. 01, 2024, Elsevier B.V. doi: 10.1016/j.coesh.2024.100533.

[16] E. Llobet, “Transition metal dichalcogenide based toxic gas sensing,” Feb. 01, 2024, Elsevier B.V. doi: 10.1016/j.coesh.2024.100533.

[17] W. Shi et al., “Tin Selenide (SnSe): Growth, Properties, and Applications,” Apr. 01, 2018, Wiley-VCH Verlag. doi: 10.1002/advs.201700602.

[18] L. D. Zhao et al., “Ultralow thermal conductivity and high thermoelectric figure of merit in SnSe crystals,” Nature, vol. 508, no. 7496, pp. 373–377, 2014, doi: 10.1038/nature13184.

[19] S. Rani, M. Kumar, H. Sheoran, R. Singh, and V. N. Singh, “Rapidly responding room temperature NO_2 gas sensor based on SnSe nanostructured film,” Mater Today Commun, vol. 30, Mar. 2022, doi: 10.1016/j.mtcomm.2022.103135.

[20] W. Yang et al., “SnSe nanosheet arrays film for trace NO_2 detection at room temperature,” Sens Actuators B Chem, vol. 370, Nov. 2022, doi: 10.1016/j.snb.2022.132407.

[21] M. Kumar et al., “Low bias operated, fast response SnSe thin film Vis-NIR photodetector on glass substrate using one-step thermal evaporation technique,” J Alloys Compd, vol. 879, Oct. 2021, doi: 10.1016/j.jallcom.2021.160370.

[22] D. Alagarasan et al., “Fabrication of SnSe nanostructures visible light photodetectors,” Inorg Chem Commun, vol. 170, Dec. 2024, doi: 10.1016/j.inoche.2024.113276.

[23] H. Yanuar, U. Lazuardi, and J. Copriady, “Preparation and characterization of thin film snse used by close spaced vapor transport technique,” 2017.

[24] G. Jeong et al., “Preparation of single-phase SnSe thin-films and modification of electrical properties via stoichiometry control for photovoltaic application,” J Alloys Compd, vol. 722, pp. 474–481, 2017, doi: 10.1016/j.jallcom.2017.06.094.

[25] Krishna. Seshan, Handbook of thin-film deposition processes and techniques: principles, methods, equipment and applications. Noyes Publications/William Andrew Pub., 2002.

[26] David M. Hata; Elena V. Brewer; And Nancy J. Louwagie “Introduction to Vacuum Technology.”

[27] Daniel. Abou-Ras, Thomas. Kirchartz, and Uwe. Rau, Advanced Characterization Techniques for Thin Film Solar Cells. Wiley-VCH, 2011.

[28] “The Basics of UV-Vis Spectrophotometry A primer.”

[29] Siderov, V. & Mladenova, D. & Yordanov, Rumen & Milenkov, V. & Ohlídal, Miloslav & Salyk, Ota & Zhivkov, I. & Weiter, Martin. (2013). Film thickness measurement by optical profilometer MicroProf® FRT. Bulgarian Chemical Communications. 45. 194-197.

[30] J. Lindemuth, “Hall Effect Measurement Handbook A Fundamental Tool for Semiconductor Material Characterization.”

[31] N. Goel, K. Kunal, A. Kushwaha, and M. Kumar, “Metal oxide semiconductors for gas sensing,” Jun. 01, 2023, John Wiley and Sons Inc. doi: 10.1002/eng2.12604.